Applied Surface Science 713 (2025) 164139

Contents lists available at ScienceDirect

Applied Surface Science

journal homepage: www.elsevier.com/locate/apsusc

Full length article

The importance of chemical transformations of adsorbed molecules for corrosion inhibition: Mercaptobenzimidazoles on copper

Anton Kokalj [a,b,*], Erik Gregori [a,b], Barbara Kapun [a], Ingrid Milošev [a,b,*]

[a] *Department of Physical and Organic Chemistry, Jožef Stefan Institute, Jamova cesta 39, SI-1000 Ljubljana, Slovenia*
[b] *Jožef Stefan International Postgraduate School, Jamova cesta 39, SI-1000 Ljubljana, Slovenia*

ARTICLE INFO

Dataset link: https://doi.org/10.17632/yrcp4jk9z7.1

Keywords:
Copper
Corrosion inhibition
Electrochemical measurements
Computational studies
Interfaces

ABSTRACT

This study investigates whether mercaptobenzimidazoles act as thiolates in inhibiting copper corrosion. To this end, we examined three mercaptobenzimidazole derivatives — 2-mercaptobenzimidazole (SH-BimH), 2-mercapto-1-methylbenzimidazole (SH-BimMe), and 2-(methylthio)benzimidazole (Me-S-BimH) — as corrosion inhibitors for copper in 3 wt% NaCl solution using a combined experimental and computational approach. Me-S-BimH has a thiol group (–SH) replaced by a methylthio group (–SCH_3), which should prevent the formation of surface thiolates. In contrast, SH-BimMe has the same molecular formula as Me-S-BimH, but its methyl group does not cap the thiol group. Corrosion experiments reveal that after 1 h of immersion, Me-S-BimH is considerably less effective than SH-BimH and SH-BimMe at inhibiting copper corrosion. However, after 100 h of immersion, Me-S-BimH performs comparably to SH-BimH and SH-BimMe. This delayed effectiveness suggests that a molecular transformation activates Me-S-BimH over time. To explore this phenomenon, we performed a detailed DFT study of potential chemical transformations of adsorbed Me-S-BimH. Most transformations are exothermic, but only molecular deprotonation and C–S bond cleavage between the azole ring and the methylthio group exhibit sufficiently low activation barriers to occur at room temperature. Similar deprotonation and C–S bond cleavage reactions occur also for SH-BimH and SH-BimMe, leading to more strongly bound species than their intact molecular forms. Due to these transformations, Me-S-BimH and SH-BimH eventually result in the same strongly bound species, while SH-BimMe forms an analogous species. These findings may explain why, over time, all three compounds exhibit similar corrosion inhibition characteristics, and highlight the importance of chemical transformations of adsorbed molecules in corrosion inhibition.

1. Introduction

Mercaptobenzimidazoles and their derivatives are efficient corrosion inhibitors for copper [1–3]. 2-mercaptobenzimidazole exists in two tautomer forms, thiol (R–SH) and thione (R=S), the latter form being by about 0.5 eV more stable [3,4]. Furthermore, the thione form also adsorbs stronger to copper surfaces than the thiol form. However, a series of adsorption studies [4–11] based on density-functional theory (DFT) reveal that the most stable adsorption form is a thiolate bonded to surface with molecular S and N atoms. Surface thiolates can form by cleaving either the S–H bond of the adsorbed thiol or the N–H bond of the adsorbed thione (thiol, thione, and thiolate forms and their relative stabilities between standalone and adsorbed forms are schematically presented in Fig. 1). This observation suggests that the active molecular species inhibiting corrosion are thiolates, which adsorb significantly stronger than the intact molecules, although adsorbed thiones may also actively participate [6].

The purpose of this study is to prove or disprove the hypothesis that the mercaptobenzimidazole's active species for inhibiting corrosion are thiolates. To this end, we performed corrosion experiments with 2-(methylthio)benzimidazole, a mercaptobenzimidazole derivative that has the thiol group (–SH) replaced with the methylthio group (–SCH_3), which prevents the transformation to a thione tautomer and should also block the formation of surface thiolates because it is much more difficult to break the S–CH_3 bond compared to the S–H or N–H bond. Note that it is known from heterogeneous catalysis that transition metals are very good X–H bond cleavers (X = C, N, S) and that X–C bond is much more difficult to cleave than the X–H bond [12]. In line with this expectation, our current corrosion experiments performed after 1 h of immersion in 3 wt% aqueous NaCl solution indeed reveal that 2-(methylthio)benzimidazole is considerably inferior to 2-mercaptobenzimidazole for inhibiting the corrosion of copper. However, experiments performed after 100 h of immersion reveal that

---

* Corresponding author at: Department of Physical and Organic Chemistry, Jožef Stefan Institute, Jamova cesta 39, SI-1000 Ljubljana, Slovenia.
E-mail addresses: tone.kokalj@ijs.si (A. Kokalj), ingrid.milosev@ijs.si (I. Milošev).
URLs: http://www.ijs.si/ijsw/K3-en/Kokalj (A. Kokalj), http://www.ijs.si/ijsw/K3-en/Milosev (I. Milošev).

https://doi.org/10.1016/j.apsusc.2025.164139
Received 30 April 2025; Received in revised form 21 July 2025; Accepted 22 July 2025

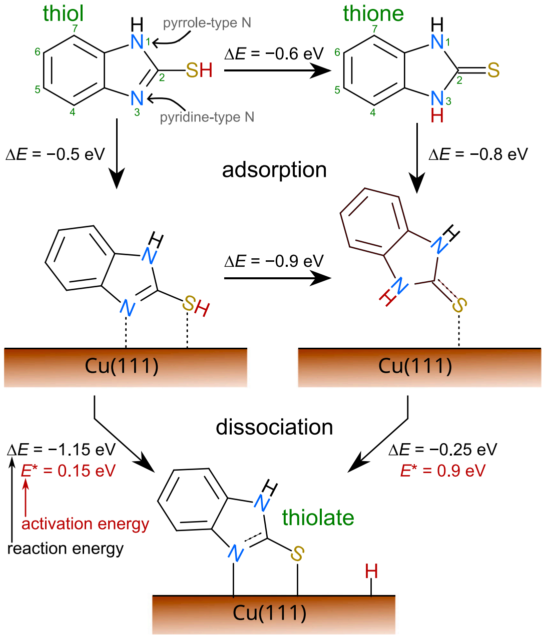

Fig. 1. Schematic representation of thiol and thione tautomers of 2-mercaptobenzimidazole as going from gas-phase to adsorbed state, and finally to a "dissociated" thiolate state on Cu(111). ΔE designates the energy difference between two different states, whereas dissociation barriers are indicated by E^*. ΔE and E^* values are taken from Ref. [4].

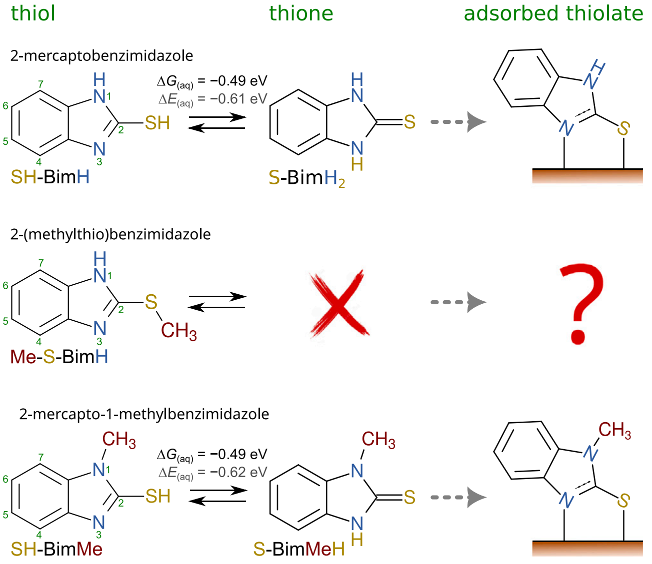

Fig. 2. Skeletal structures of the three considered inhibitor compounds in thiol, thione, and adsorbed thiolate forms; the corresponding shortcut labels are also indicated (Bim stands for the benzimidazole fragment and Me for the methyl group). The choice of 2-(methylthio)benzimidazole (Me-S-BimH) is based on the chemically intuitive assumption that it cannot form thiolate because it has the S atom *passivated* by the methyl group; furthermore, it also cannot exist in the thione form. $\Delta E_{(aq)}$ ($\Delta G_{(aq)}$) stands for the (standard Gibbs) energy difference between the thione and thiol forms solvated in the aqueous solvent; these values are taken from Ref. [3] and correspond to the DFT calculated values.

2-(methylthio)benzimidazole is as good as 2-mercaptobenzimidazole and 2-mercapto-1-methylbenzimidazole. This latter observation implies that either the hypothesis that thiolates are the active species inhibiting corrosion is wrong or that some other molecular chemical transformation activates the 2-(methylthio)benzimidazole molecules. To shed some light onto this interesting question, we performed a detailed DFT study of several potential transformations of adsorbed molecules to scrutinize their viability and to establish whether some of them result in sufficiently strong adsorbed molecules to persist on the surface for prolonged time, which is a prerequisite for adsorption-type inhibitors to inhibit corrosion.

2. Technical details

2.1. Inhibitors and their labels

Three mercaptoazole compounds were tested as corrosion inhibitors for copper in 3 wt% aqueous NaCl solutions. In particular, in addition to the parent 2-mercaptobenzimidazole (labeled as SH-BimH) and its 2-(methylthio)benzimidazole (Me-S-BimH) derivative mentioned in the introduction, 2-mercapto-1-methylbenzimidazole (SH-BimMe) was considered, which has the same molecular formula as 2-(methylthio)benzimidazole, $C_8H_8N_2S$, but differs in the position of the methyl group. The skeletal formulae of the three molecules, their tautomeric forms, and shorthand labels are presented in Fig. 2; these labels are taken from Ref. [3], where the labeling nomenclature was also explained. With this labeling scheme, the thiol, thione, and thiolate forms of 2-mercaptobenzimidazole are labeled as SH-BimH, S-BimH$_2$, and S-BimH, respectively, and likewise for the other two molecules. In this labeling scheme, Bim denotes the benzimidazole moiety, while Me refers to the methyl group.

2.2. Experimental

The utilized experimental procedure is compatible with the one described in Ref. [3]. Corrosion tests were conducted on copper metal (99.9% purity), purchased from Goodfellow (Cambridge Ltd., UK) in the form of a 2 mm thick sheet. Disc-shaped specimens with a diameter of 15 mm were cut from the sheet and mechanically ground using a rotating plate polisher. The grinding was performed with SiC papers using progressively finer gradations of 500, 800, 1000, 1200, 2400, and finally 4000. Copper samples were then cleaned with ethanol in an ultrasonic bath for three minutes, rinsed with distilled water, and dried with nitrogen gas. The samples were immersed in 3 wt% aqueous NaCl solutions with or without an inhibitor at a concentration of 1 mM. The performance of inhibitors was then assessed with potentiodynamic polarization and linear polarization resistance (LPR) measurements. Each measurement was repeated at least three times.

Electrochemical measurements were conducted in three-electrode corrosion cells (volume 0.25 L, Autolab, Ecochemie, Netherlands) at 25 °C using a multichannel potentiostat/galvanostat Autolab Model M204 (Metrohm Autolab, Utrecht, Netherlands) operated with Nova 2.1 software. As a reference electrode, a saturated calomel electrode (SCE, 0.242 V relative to the standard hydrogen electrode at 25 °C) with a Luggin capillary was used. A specimen embedded in a Teflon holder, with an area of 0.785 cm^2 exposed to the solution, served as the working electrode. Carbon rods were used as the counter electrode. All potentials in this article are given relative to the SCE scale.

Two sets of potentiodynamic polarization measurements were conducted: the first after 1 h and the second after 100 h of immersion. A potential scan rate of 1 mV/s was employed, commencing 250 mV below the open circuit potential (OCP) and progressing in the anodic direction. To ensure reliability and accuracy, a minimum of three measurements were performed for each sample at each specific time of immersion (1 h or 100 h), and the most representative measurement was selected for graphical presentation. Measurements for each specific immersion time were conducted on separate samples. From these data, the electrochemical corrosion parameters — i.e., the corrosion potential (E_{corr}) and corrosion current density (j_{corr}) — were determined by Tafel extrapolation using Nova 2.1 software, along with their associated standard deviations.

To shed light on the behavior of the inhibitors between 1 h and 100 h of immersion, the LPR measurements were performed at specific times of 1, 2, 3, 5, 24, 48, 72, and 100 h. A potential range of ±10 mV relative to the OCP with a scan rate of 0.1 mV/s was used. The polarization resistance (R_p) values were determined from the fitted slope on the potential vs. the current density plot. Measurements were repeated at least three times for each inhibitor, and at each discrete time, the resulting R_p values were averaged as:

$$\langle R_\mathrm{p}(t_k)\rangle = \frac{1}{m}\sum_{i}^{m} R_\mathrm{p}^{(\mathrm{i})}(t_k), \tag{1}$$

where m is the number of measurements and $R_\mathrm{p}^{(\mathrm{i})}(t_k)$ is the ith measurement value of R_p at a discrete time t_k.

2.3. *Computational*

DFT calculations were performed with the Quantum ESPRESSO open-source software package [13,14]. We used the PBE+D” method [15] that consists of the Perdew–Burke–Ernzerhof (PBE) functional [16] and a modified D2 empirical dispersion correction of Grimme [17], with the C_6 parameter of Cu reparametrized from the original value of 375 Ry/Bohr^6 to the value of 140 Ry/Bohr^6 [15] to reduce the molecule–surface overbinding of the original PBE+D2 method [18–20]. Kohn–Sham orbitals were expanded in a plane-wave basis set using a kinetic energy cutoff of 30 Ry and 240 Ry for wave-functions and density, respectively. The PWTK scripting [21] environment was utilized to automate computational workflows. Molecular graphics were produced with the XCrySDen graphical package [22], and post-processing of figures was done in Inkscape [23].

All results presented in this work correspond to *in-vacuo* calculations performed with the Cu(111)–(4 × 4) supercell. Cu(111) was described by a slab consisting of four (111) layers. The bottom layer was constrained to the bulk positions in accordance with the calculated equilibrium Cu bulk lattice parameter of 3.65 Å [6]. The special point technique [24] with Methfessel–Paxton [25] smearing of 30 mRy and a shifted 4 × 4 × 1 k-point mesh was employed for the Brillouin-zone integration of the Cu(111)–(4 × 4) supercell.

In real environments, metal surfaces are never clean. Even during active dissolution, they are covered with adsorbed species such as O, OH, H, and Cl [26]. Hence, as an oversimplified surface model, we used the O/Cu(111)–(4 × 4) model, i.e., a Cu(111) surface containing one O adatom per (4 × 4) supercell. In cases requiring more oxygen, we use the 2O/Cu(111)–(4 × 4) surface model. These surface models evolve during chemical reactions. For example, during molecular deprotonation, MolH@O/Cu(111)–(4 × 4) transforms into Mol@OH/Cu(111)–(4 × 4), where MolH and Mol designate an intact and deprotonated molecule, respectively.

Reaction activation energies were calculated with the climbing-image nudged-elastic band (CI-NEB) method [27,28], where a reaction is modeled as a minimum-energy path (MEP) between an initial state (IS) and a final state (FS). The transition state (TS) is the maximum-energy configuration on the MEP, and the activation energy (E^*) is calculated as the difference between the TS and IS energies:

$$E^* = E_\mathrm{TS} - E_\mathrm{IS}. \tag{2}$$

The energy change during reaction (i.e., *reaction energy*) was calculated as the difference between the total energies of products and reactants, i.e.:

$$\Delta E = E_\mathrm{products} - E_\mathrm{reactants}, \tag{3}$$

which can also be written as:

$$\Delta E = E_\mathrm{FS} - E_\mathrm{IS}. \tag{4}$$

Table 1
Corrosion potentials (E_corr) and corrosion current densities (j_corr), along with their associated standard deviations, deduced from the potentiodynamic polarization curves (see representative examples in Fig. 3) for copper in 3 wt% NaCl solution with and without 1 mM inhibitor.

	E_corr (V vs. SCE)	j_corr (μA cm^{-2})
	after 1 h of immersion	
NaCl	−0.244 ± 0.012	1.573 ± 0.169
SH-BimH	−0.204 ± 0.037	0.039 ± 0.013
SH-BimMe	−0.216 ± 0.015	0.045 ± 0.007
Me-S-BimH	−0.318 ± 0.019	0.397 ± 0.081
	after 100 h of immersion	
NaCl	−0.214 ± 0.059	1.357 ± 1.263
SH-BimH	−0.173 ± 0.023	0.046 ± 0.050
SH-BimMe	−0.176 ± 0.010	0.006 ± 0.003
Me-S-BimH	−0.140 ± 0.075	0.002 ± 0.0002

The adsorption binding energy (E_b) of an adsorbed molecular species was calculated as:

$$E_\mathrm{b} = E_{\mathrm{mol@X/Cu(111)}} - E_\mathrm{mol} - E_{\mathrm{X/Cu(111)}}, \tag{5}$$

where the label “mol” denotes a molecular species, while “mol@X/Cu(111)” represents the molecular species adsorbed on the X/Cu(111) surface model (X = O, OH…). Spin-polarized calculations of “mol” were performed for cases where “mol” is a molecular radical.

An extensive configurational search was performed to identify low-energy IS, TS, and FS structures. In this study, we considered ten qualitatively different adsorbed molecular species, eleven distinct chemical reactions, and nine different copper substrates based on O/Cu(111); note that the considered reactions generate various X/Cu(111) and (X+Y)/Cu(111) possibilities.[1] In total, over 160 relaxation calculations of adsorbed structures and 47 CI-NEB reaction-path calculations were performed.

3. Results

3.1. *Experimental results*

The primary hypothesis being tested herein is that mercaptobenzimidazoles are active against corrosion in their thiolate form. For this reason, we performed experiments with the Me-S-BimH compound, a derivative of SH-BimH, whose molecular structure has the S atom capped by the methyl group[2] that should prevent the formation of thiolates. Consequently, the Me-S-BimH compound should not be an efficient inhibitor. In contrast, the SH-BimMe compound, having the same molecular formula as Me-S-BimH but differing in the position of the methyl group, can form thiolates and should be an efficient inhibitor.

3.1.1. *Potentiodynamic polarization curves*

Representative potentiodynamic polarization curves for copper in 3 wt% NaCl solution with and without 1 mM of SH-BimH, SH-BimMe, or Me-S-BimH, measured after 1 h and 100 h of immersion, are shown in Fig. 3. The corresponding corrosion potentials and corrosion current densities, along with their associated standard deviations, as deduced from the potentiodynamic polarization measurements, are presented in Table 1.

---

[1] The considered substrates are: O/Cu(111), OH/Cu(111), (O+OH)/Cu(111), OMe/Cu(111), (S+O)/Cu(111), (S+OH)/Cu(111), (SMe+O)/Cu(111), (OMe+OH)/Cu(111), (SMe+OH)/Cu(111), as well as pristine Cu(111).

[2] Specifically, the hydrogen atom of the thiol group (–SH) is replaced with a methyl group, forming a methylthio group (–SCH$_3$), which is expected to prevent the thiol from acting as a reactive site for thiolate formation.

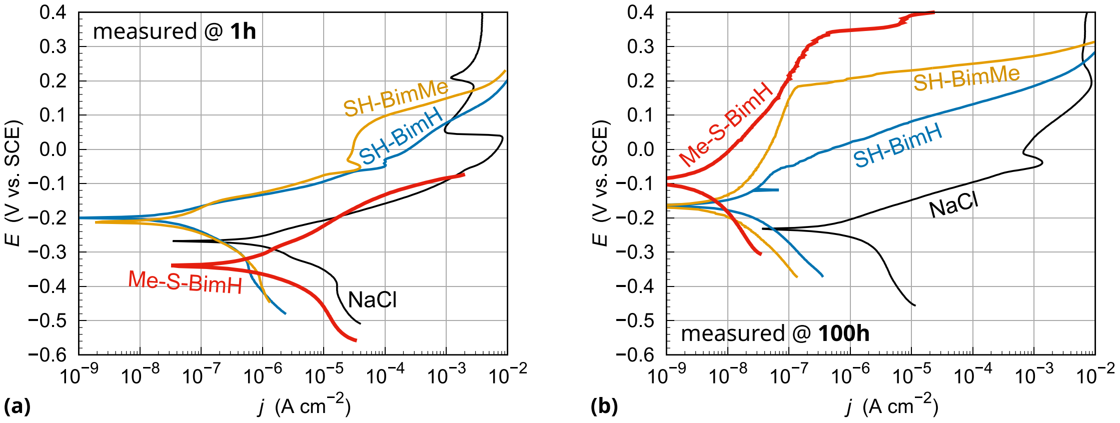

Fig. 3. Potentiodynamic polarization curves for copper in 3 wt% NaCl solution with and without 1 mM of the SH-BimH, SH-BimMe, or Me-S-BimH compound, measured at (a) 1 h and (b) 100 h of immersion with the scan rate of 1 mV/s.

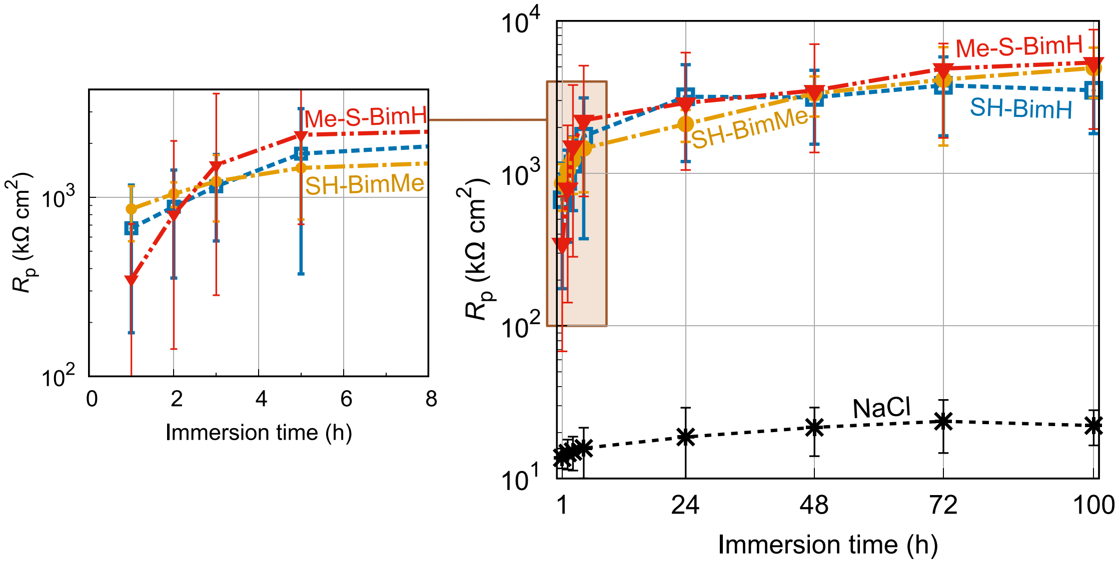

Fig. 4. Average polarization resistance (R_p) measured at discrete times (points) over a 100 h interval for copper in a 3 wt% NaCl solution, with and without the addition of 1 mM SH-BimH, SH-BimMe, or Me-S-BimH; note the logarithmic scale of R_p. Each point represents the average R_p value at a given discrete time, obtained from multiple measurements, i.e., it corresponds to $\langle R_p^{\mathrm{inh}}(t_k)\rangle$ of Eq. (1). Error bars are included to indicate the variability of the measurements. The inset on the left provides a magnified view of the R_p results for the inhibited samples during the first several hours of immersion.

The reactions indicated by the polarization curve recorded after 1 h of immersion in blank NaCl (Fig. 3a) have been discussed previously [2,11]. In a near-neutral NaCl solution, the primary cathodic reaction is oxygen reduction, whereas the anodic reaction involves the formation of soluble cuprous chloride complexes,[3] $CuCl_2^-$, which promote copper dissolution at potentials above the corrosion potential. Due to this process, a passive range cannot be established. Consequently, the current density increases exponentially above the corrosion potential, reaching a peak of nearly 10^{-2} A cm^{-2} at around 0.05 V. The subsequent decrease in current density at more positive potentials, down to approximately 10^{-3} A cm^{-2}, is attributed to the formation of CuCl, followed by the dissolution and the transformation of cuprous to cupric ions.

Adding SH-BimH and SH-BimMe to the NaCl solution causes the following changes in the polarization response measured after 1 h of immersion (Fig. 3a): the current density in the cathodic branch is reduced by approximately one order of magnitude, and the corrosion potential shifts positively by about 0.1 V. Above the corrosion potential, the current density continues to increase as in blank NaCl, but reaches significantly lower values due to the positive shift in the corrosion potential. Therefore, SH-BimH and SH-BimMe act as mixed-type inhibitors, with a stronger effect on the anodic branch. The shape of the anodic branches differs from that observed in blank NaCl. For SH-BimH, only a hint of the current peak appears around −0.05 V at 10^{-4} A cm^{-2}, followed by an increase in current density. For SH-BimMe, the current peak forms at even lower current densities, around $10^{-4.5}$ A cm^{-2}, followed by a passive current plateau and an abrupt increase at approximately 0.1 V. These differences indicate that the course of the anodic process is altered in the presence of the inhibitors, and that the formation of cupric ions does not occur [2,11]. As shown in our previous studies using X-ray photoelectron spectroscopy (XPS), the addition of SH-BimH and SH-BimMe results in the formation of a Cu–inhibitor layer [2,11,29], which suppresses the dissolution of Cu in chloride-containing solution and thus acts as a strong anodic inhibitor, particularly in the case of SH-BimMe.

Potentiodynamic polarization curves recorded after 1 h of immersion in NaCl with Me-S-BimH added (Fig. 3a) show different behavior. While SH-BimMe and SH-BimH shift the corrosion potential by about 0.1 V in the anodic direction relative to the sample immersed in bare

---

[3] In contrast, in the absence of chloride ions, the preferred anodic reaction in a near-neutral solution is the formation of cuprous oxide.

NaCl solution, Me-S-BimH shifts it in the cathodic direction by a similar amount, and its effect on the current density in the cathodic branch is weaker than that of SH-BimH and SH-BimMe. Moreover, the SH-BimMe and SH-BimH curves are left-shifted by more than one order of magnitude in current density compared to the NaCl curve, whereas the curve for Me-S-BimH remains similar to that of blank NaCl and follows the same trend in the anodic branch. These contrasting behaviors are also reflected in the corrosion current densities reported in Table 1. Thus, polarization experiments conducted after 1 h of immersion reveal that Me-S-BimH is a weak inhibitor, considerably inferior to SH-BimH and SH-BimMe, supporting the initial hypothesis that it is unable to transform into a thiolate and form a protective inhibitor layer.

In contrast, potentiodynamic polarization curves recorded after 100 h of immersion (Fig. 3b) reveal a remarkably different behavior. The performance of all three inhibitors is considerably better than that measured after 1 h of immersion because the curves are strongly left-shifted to more positive potentials and lower current densities (see also Table 1). Me-S-BimH is as efficient as SH-BimMe, if not more efficient. Both surpass SH-BimH and exhibit notable barrier-type corrosion protection. This result implies that either the hypothesis that thiolates are the active species inhibiting corrosion is incorrect or that some other molecular chemical transformation activates the Me-S-BimH compound. The fact that Me-S-BimH is very effective after 100 h but not after 1 h of immersion seems to favor the latter assumption because it suggests that the relevant chemical transformation is sufficiently activated and requires some time to occur.

3.1.2. Linear polarization resistance

To shed some light on the behavior of the three inhibitor compounds between 1 h and 100 h of immersion, we also performed non-destructive LPR measurements at 1, 2, 3, 5, 24, 48, 72, and 100 h of immersion (Fig. 4). The LPR measurements confirm that at 1 h of immersion, Me-S-BimH is inferior to SH-BimMe and SH-BimH because it displays approximately two times lower R_p value than the other two inhibitors. For all three inhibitors, the R_p values increase rapidly from 1 to 5 h, and then the rate of increase slows significantly. In the time range from 48 to 100 h, the R_p values of Me-S-BimH and SH-BimMe are similar, and at 100 h of immersion, both outperform SH-BimH, in agreement with the results of potentiodynamic measurements (Fig. 3b). After 100 h of immersion, all three inhibitors exceed the results in blank NaCl by more than two orders of magnitude.

The observation that the inhibition performance of all three inhibitors increases rapidly within the first 5 h of immersion suggests that an activated chemical process transforms them into a more effective form. Moreover, the fact that Me-S-BimH exhibits a distinctly different evolution of corrosion parameters over time — namely, a delayed increase in R_p, a delayed decrease in j_{corr}, and a more positive shift in E_{corr} (Figs. 3 and 4, and Table 1) — suggests that the associated adsorption process follows a different pathway compared to SH-BimH and SH-BimMe. To investigate this further, we now turn to computational results and examine several potential chemical transformations of the adsorbed molecules to evaluate their feasibility and to determine, particularly for Me-S-BimH, whether any of them yield sufficiently stable adsorbed species capable of persisting on the surface over time—a prerequisite for effective corrosion inhibition by adsorption-type inhibitors.

3.2. Chemical transformations of Me-S-BimH

In this section, potentially viable molecular transformations of Me-S-BimH are considered using DFT calculations. The schematics of these reactions with the corresponding snapshots of the most stable identified initial-, transition-, and final-state structures are presented in Figs. 5–8.

As mentioned in the Technical section, an extensive configurational search was performed to identify low-energy IS, TS, and FS structures, which involved over 160 relaxation calculations of adsorbed structures and 47 CI-NEB reaction-path calculations. To this end, various adsorption sites, molecular orientations, and relative positions of the azole molecular species with respect to X coadsorbates (X = O, OH, OMe, SMe…) were explored. While it cannot be guaranteed that the lowest energy structures were found, the diversity of considered configurations ensures that at least reasonably stable structures were identified. Hence, only the most stable identified structures and their corresponding energies are presented below. In contrast, Figs. S1–S7 in the Supplementary material also present complementary IS, TS, and FS structures, where “complementary” refers to configurations that are characteristically different from the most stable identified ones.

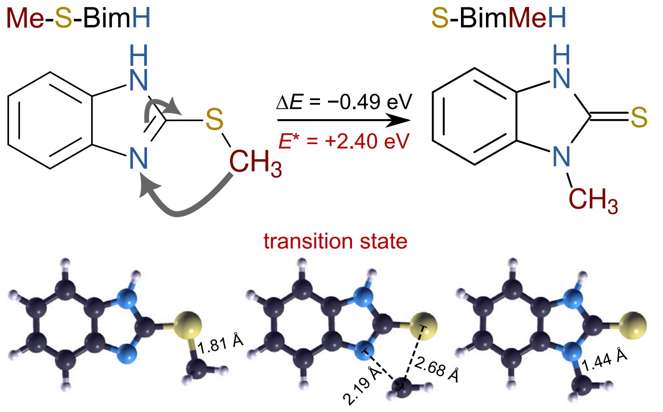

Fig. 5. Top: schematic of the intraconversion of standalone Me-S-BimH into S-BimMeH, involving the shift of the methyl group from the S atom to the pyridyne-type N atom and a transformation of the C=N–S bonding motif into N–C=S. The corresponding activation and reaction energies are also stated. Bottom: snapshots of the IS, TS, and FS structures.

3.2.1. Can Me-S-BimH transform to S-BimMeH?

The observation that from 48 to 100 h of immersion, the R_p values of Me-S-BimH and SH-BimMe are similar (Fig. 4) may suggest that Me-S-BimH transforms to the SH-BimMe structural isomer, in particular to the S-BimMeH thione tautomer, i.e.:

$$\text{Me-S-BimH} \rightarrow \text{S-BimMeH}. \tag{6}$$

This reaction involves a shift of the methyl group from the S atom to the pyridyne-type N atom and a transformation of the C=N–S to the N–C=S bonding motif (Fig. 5). For standalone molecules, the calculated reaction is exothermic ($\Delta E = -0.5$ eV), but the activation energy ($E^* = 2.4$ eV) is way too high for reaction to be feasible at room temperature.

3.2.2. Can deprotonated Me-S-Bim transform to deprotonated S-BimMe?

However, for adsorbed molecules, another two-step reaction is possible. First, the N–H bond of adsorbed Me-S-BimH is cleaved with the aid of a nearby adsorbed O atom. In the subsequent step, the methyl group shifts from the S atom to the N atom, i.e.:

$$\text{Me-S-BimH}_{(ads)} + \text{O}_{(ads)} \rightarrow \text{Me-S-Bim}_{(ads)} + \text{OH}_{(ads)}, \tag{7}$$

followed by:

$$\text{Me-S-Bim}_{(ads)} + \text{OH}_{(ads)} \rightarrow \text{S-BimMe}_{(ads)} + \text{OH}_{(ads)}. \tag{8}$$

The schematics of the two reaction steps, along with the calculated reaction and activation energies, are shown in Fig. 6, accompanied by snapshots of the most stable identified IS, TS, and FS structures. Both reaction steps are exothermic with the respective reaction energies of −0.22 and −0.87 eV. While the first step has a negligible activation barrier of 0.02 eV, the activation barrier of the second step (1.87 eV) is too high for the reaction to be viable at room temperature.

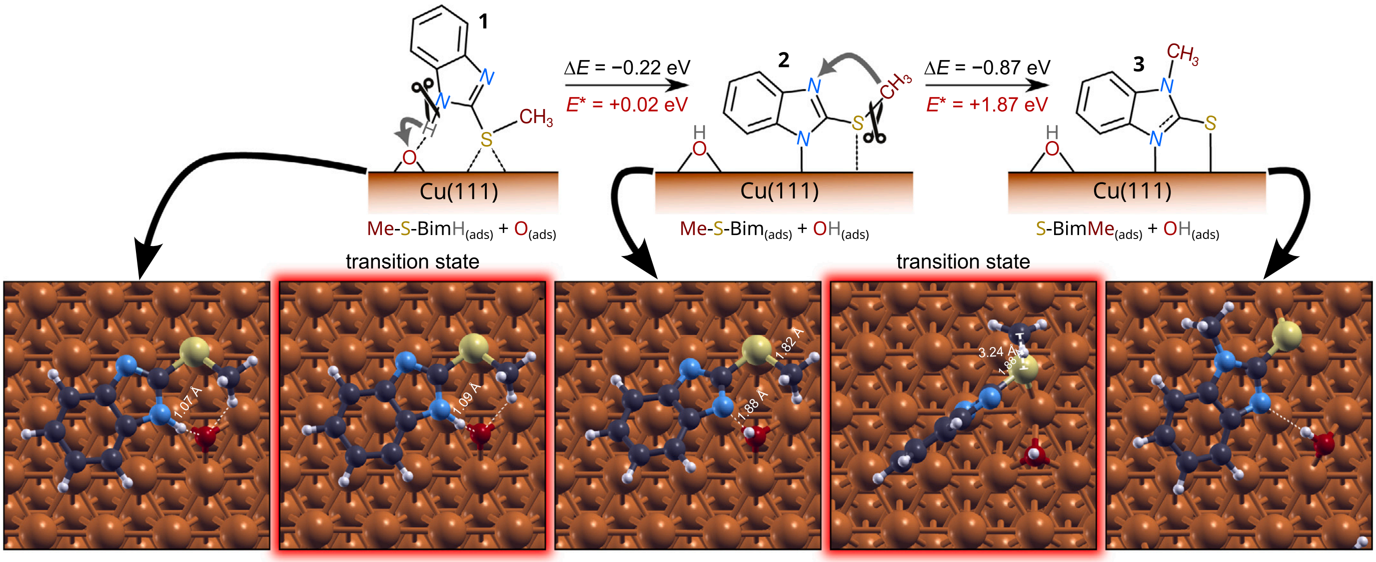

Fig. 6. Top: schematic representation of the $O_{(ads)}$-assisted deprotonation of Me-S-$BimH_{(ads)}$, reaction (7), and the subsequent interconversion of Me-S-$Bim_{(ads)}$ into S-$BimMe_{(ads)}$, involving the shift of the methyl group from S to the pyridyne-type N atom, reaction (8). The corresponding activation and reaction energies are also provided, while the bold numbers indicate the adsorbed molecular species (these identifiers are occasionally referenced in the text). Bottom: snapshots of the most stable identified IS, TS, and FS structures.

3.2.3. Dissociative adsorption of Me-S-BimH via the C–S bond cleavage

In addition to the above-discussed reactions, we also investigated two dissociation reactions of adsorbed Me-S-BimH that involve the C–S bond cleavage, in particular, the bond within the methylthio group (S–CH_3) and the bond between the azole ring and the methylthio group (C–SCH_3). The two reactions can be written as:

$$\text{Me-S-BimH}_{(ads)} + \text{O}_{(ads)} \rightarrow \text{S-BimH}_{(ads)} + \text{OMe}_{(ads)}, \tag{9}$$

$$\text{Me-S-BimH}_{(ads)} \rightarrow \text{BimH}^{(C2)}_{(ads)} + \text{SMe}_{(ads)}, \tag{10}$$

where the "(C2)" superscript in the $\text{BimH}^{(C2)}_{(ads)}$ label indicates that the exocyclic bond at the molecular C2 atom was cleaved. The skeletal representations of the two reactions are shown in Fig. 7, along with the calculated reaction and activation energies and the most stable identified IS, TS, and FS structures.

Concerning the reaction involving the cleavage of the S–CH_3 bond, the released methyl can bind to either $O_{(ads)}$ forming an adsorbed methoxy group (OCH_3), labeled as $OMe_{(ads)}$ in reaction (9), or to the copper surface forming an adsorbed methyl group (Me). Because the adsorbed $OMe_{(ads)}$ is 0.56 eV more stable than the coadsorbed $O_{(ads)}$ + $Me_{(ads)}$, we considered only the reaction forming $OMe_{(ads)}$, that is, reaction (9). The respective activation energy is 1.47 eV, and the reaction is exothermic with $\Delta E = -0.76$ eV (Fig. 7a). This activation energy is relatively high, making the reaction impractical at room temperature.

As for the cleavage of the other C–S bond, reaction (10), the cleavage of the C–SCH_3 bond between the azole ring and the methylthio group proceeds with the calculated activation energy of 0.85 eV and a moderately exothermic reaction energy of $\Delta E = -0.44$ eV (Fig. 7b). This barrier is low enough to make the C–SCH_3 bond dissociation kinetically feasible at room temperature.

The above results imply that the cleavage of the C–SCH_3 bond is kinetically much faster, although thermodynamically less favorable than the cleavage of the S–CH_3 bond.

3.2.4. The C–S bond cleavages of deprotonated Me-S-Bim

As described above, deprotonation of adsorbed Me-S-BimH, reaction (7), is calculated to be kinetically fast ($E^* = 0.02$ eV) and thermodynamically favored ($\Delta E = -0.22$ eV), implying easy formation of Me-S-$Bim_{(ads)}$. Therefore, it is prudent to also consider the two C–S bond cleavages (S–CH_3 and C–SCH_3) of deprotonated Me-S-$Bim_{(ads)}$, i.e.:

$$\text{Me-S-Bim}_{(ads)} + \text{O}_{(ads)} \rightarrow \text{S-Bim}_{(ads)} + \text{OMe}_{(ads)}, \tag{11}$$

$$\text{Me-S-Bim}_{(ads)} \rightarrow \text{Bim}^{(C2)}_{(ads)} + \text{SMe}_{(ads)}. \tag{12}$$

The schematics of these reactions are shown in Fig. 8 along with the calculated reaction and activation energies and the most stable identified IS, TS, and FS structures.

The S–CH_3 bond cleavage of deprotonated Me-S-$Bim_{(ads)}$, reaction (11), is moderately exothermic with $\Delta E = -0.37$ eV. However, the calculated activation energy of 2.11 eV is way too high for reaction to occur at room temperature. The other bond dissociation, i.e., the C–SCH_3 bond cleavage of reaction (12), is not even exothermic (ΔE = 0.03 eV), although it has a smaller activation barrier of 1.41 eV.

These results show that the C–S bond cleavages of deprotonated Me-S-$Bim_{(ads)}$ are not feasible. Further evidence for this is provided by the observation that during the NEB reaction-path calculations of reaction (12), the emerging $\text{Bim}^{(C2)}_{(ads)}$ product tends to grab the proton from the nearby adsorbed OH group,[4] thus transforming into $\text{BimH}^{(C2)}_{(ads)}$. Apparently, Me-S-BimH does not prefer undergoing both N–H and C–S bond cleavages.

3.3. Chemical transformations of S-$BimH_2$ and S-BimMeH

Based on the above results, it seems worthwhile to also investigate the N–H and C–S bond dissociations of the other two molecules considered in the experimental section, 2-mercaptobenzimidazole and 2-mercapto-1-methylbenzimidazole, particularly their thione tautomers, S-$BimH_2$ and S-BimMeH.

---

[4] This OH group forms in the preceding deprotonation reaction (7). The tendency of the emerging $\text{Bim}^{(C2)}_{(ads)}$ product to grab the proton is so strong that the O–H bond distance of the nearby adsorbed OH group needs to be constrained.

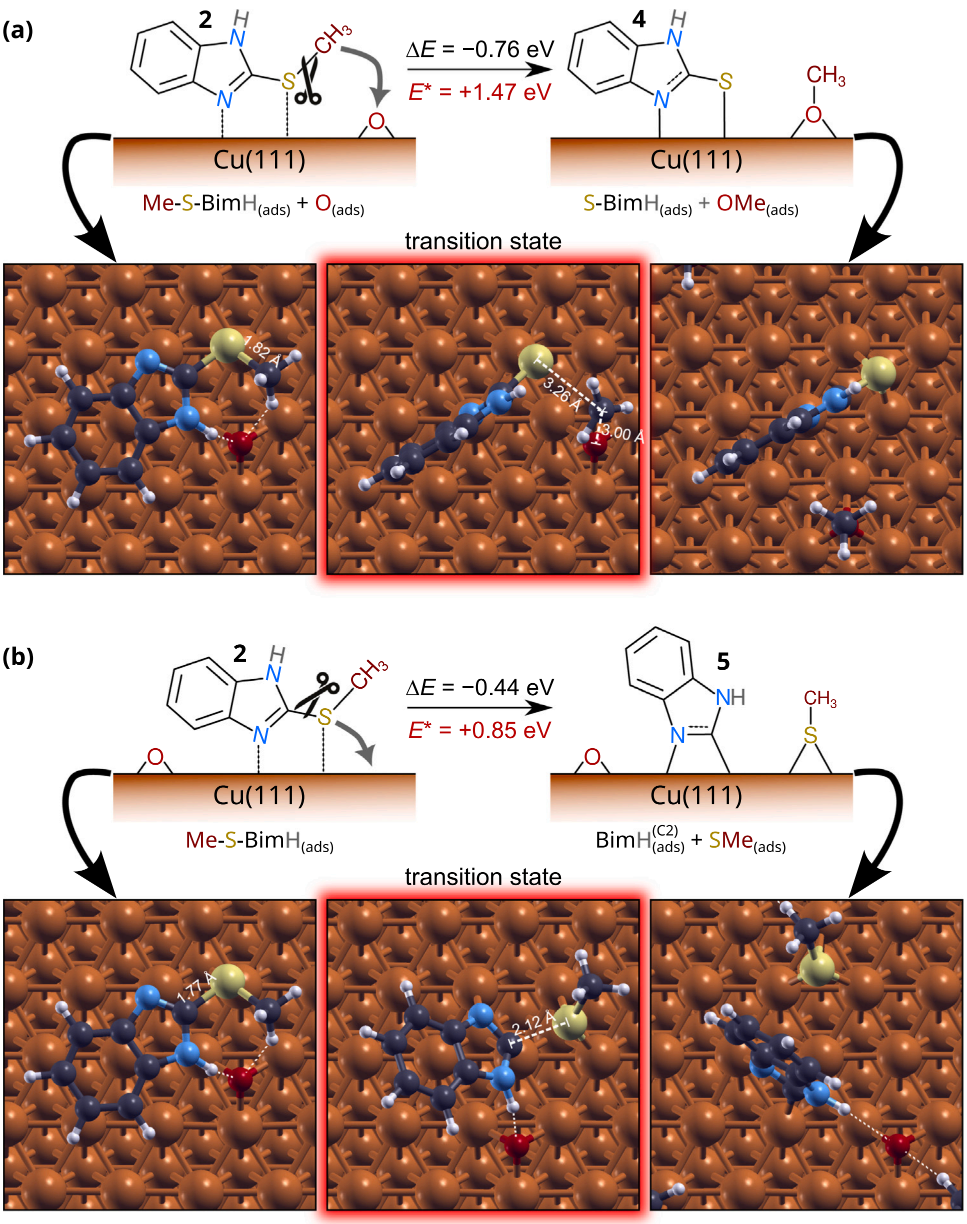

Fig. 7. Schematics and the corresponding snapshots of the two possible C–S bond cleavages of Me-S-BimH$_{(ads)}$: (a) the S–CH$_3$ bond cleavage, reaction (9), and (b) the C–SCH$_3$ bond cleavage, reaction (10). The corresponding activation and reaction energies are also stated, while the bold numbers indicate the assigned identifiers of the adsorbed molecular species.

3.3.1. The N–H bond cleavages

The activation energies for the N–H bond cleavage of azoles on bare Cu(111), such as mercaptobenzimidazole and benzotriazole, are about 1 eV [4,30]. However, as shown above, O$_{(ads)}$ promotes the N–H bond dissociation to such an extent that the activation barrier becomes negligible. Furthermore, we demonstrated in a previous publication [31] that O$_{(ads)}$ and OH$_{(ads)}$ reduce the activation barrier for the N–H bond cleavage of benzotriazole on Cu(111) to an exceedingly small value of 0.01 eV. Minute or even vanishing N–H dissociation barriers were also reported [32] for triazole and tetrazole on Cu$_2$O surfaces near oxygen vacancies (where the role of oxygen vacancy is to allow the deprotonated azole to form at least two N–Cu bonds).

As for S-BimH$_2$ and S-BimMeH, the respective N–H bond dissociations can be written as:

$$\text{S-BimH}_{2(ads)} + \text{O}_{(ads)} \rightarrow \text{S-BimH}_{(ads)} + \text{OH}_{(ads)}, \tag{13}$$

$$\text{S-BimMeH}_{(ads)} + \text{O}_{(ads)} \rightarrow \text{S-BimMe}_{(ads)} + \text{OH}_{(ads)}. \tag{14}$$

The schematics of these reactions, along with the calculated reaction and activation energies, are shown in the left part of Fig. 9, accompanied by snapshots of the most stable identified IS, TS, and FS structures. These N–H bond dissociations typically proceed in two steps. In the first step, the N–H bond is cleaved by proton transfer from N–H to O$_{(ads)}$, transforming the N–H⋯O hydrogen bond into the N⋯H–O one. This step exhibits vanishing activation barriers of 0.01 and 0.02 eV for S-BimH$_2$ and S-BimMeH, respectively. In the second step, the newly formed thiolate rearranges into a more stable structure that bonds to the surface with the N and S atoms. The resulting thiolates are about 0.3 eV more stable than the intact adsorbed molecules.

3.3.2. The C–S bond cleavages of S–BimH and S–BimMe

Having established above that the C–S bond cleavage between the azole ring and the methylthio group is feasible for Me-S-BimH$_{(ads)}$, it

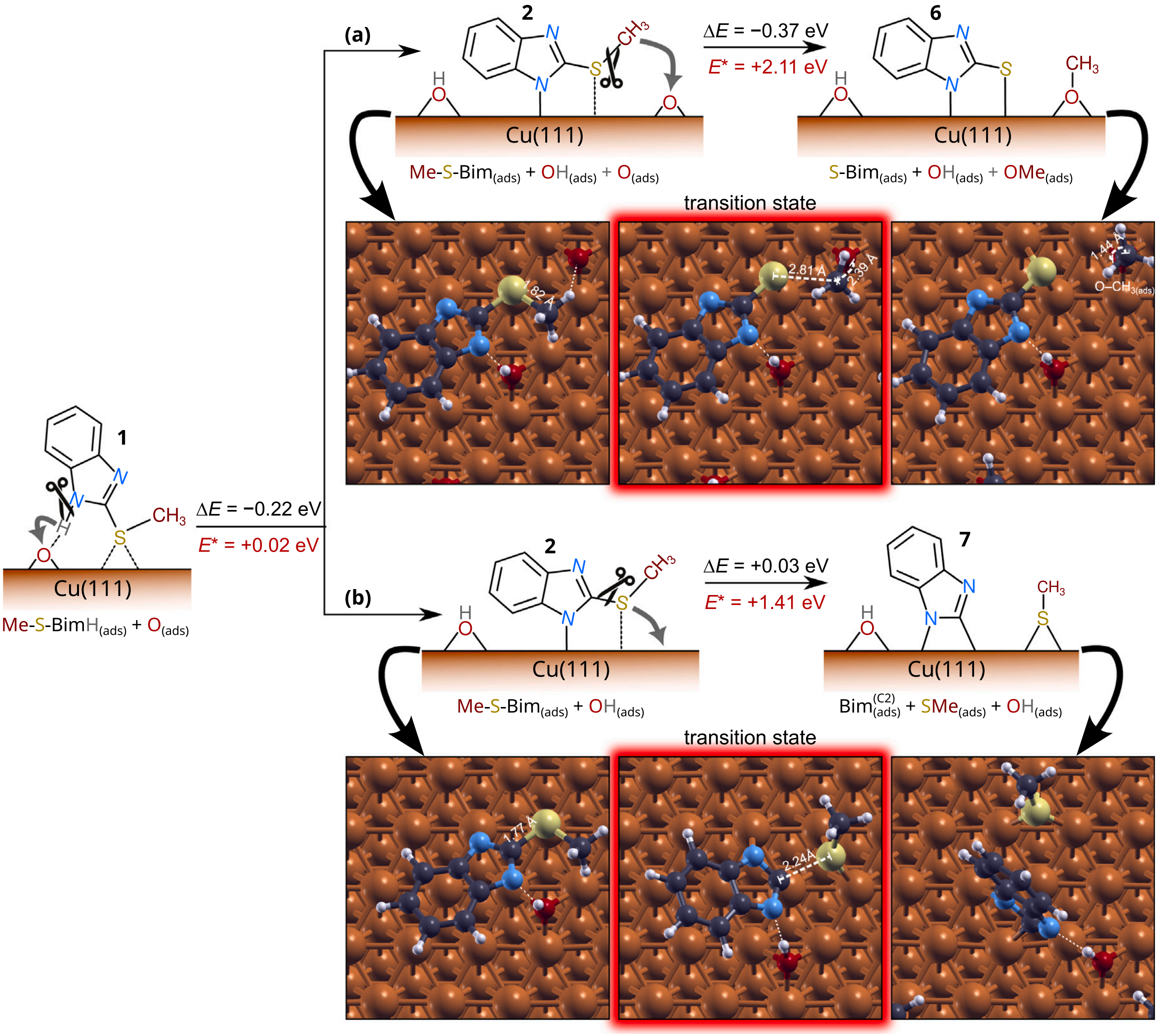

Fig. 8. Schematic representation of the $O_{(ads)}$-assisted deprotonation of Me-S-$BimH_{(ads)}$, forming Me-S-$Bim_{(ads)}$, followed by two possible subsequent C–S bond cleavages of Me-S-$Bim_{(ads)}$: (a) S–CH_3 bond cleavage within the methylthio group, reaction (11), and (b) C–SCH_3 bond dissociation, reaction (12). The corresponding activation and reaction energies, along with snapshots of the most stable identified IS, TS, and FS structures, are also presented. The bold numerals denote the assigned identifiers of the adsorbed molecular species.

seems reasonable to assess its feasibility for 2-mercaptobenzimidazole and 2-mercapto-1-methylbenzimidazole as well. To this end, we considered only the thiolates[5] formed in reactions (13) and (14). The respective reactions are:

$$\text{S-BimH}_{(ads)} \rightarrow \text{BimH}^{(C2)}_{(ads)} + \text{S}_{(ads)}, \tag{15}$$

$$\text{S-BimMe}_{(ads)} \rightarrow \text{BimMe}^{(C2)}_{(ads)} + \text{S}_{(ads)}. \tag{16}$$

The skeletal representations of these reactions are shown in the right part of Fig. 9, along with the calculated reaction and activation energies and the most stable identified IS, TS, and FS structures. For both molecules, the C–S bond cleavages are calculated to be moderately exothermic, by about 0.4 eV, and kinetically feasible at room temperature, with activation barriers of 0.99 eV and 0.84 eV for S-BimH and S-BimMe, respectively.

The finding that adsorbed 2-mercaptobenzimidazole may undergo C–S bond cleavage is supported by experimental observations. Specifically, the appearance of atomic S resulting from molecular decomposition of 2-mercaptobenzimidazole on Cu(111) was evidenced by the formation of a (7 × 7)R19.1° superstructure observed via scanning tunneling microscopy [33]. This superstructure is characteristic of atomic S adsorption on Cu(111) [34]. Furthermore, a similar presence of atomic S was also observed for 2-mercaptobenzothiazole, a structurally related compound in which one endocyclic N atom is replaced by an S atom [35], further supporting the propensity of such molecules to undergo C–S bond cleavage upon adsorption.

4. Discussion

Adsorption and surface reactions — specifically C–N bond formation, and N–H and C–S bond cleavages — of three different molecules (Me-S-BimH, S-$BimH_2$, and S-BimMeH) were considered above, resulting in ten qualitatively distinct adsorbed molecular species, denoted as **1**–**10** in Figs. 6–9. Most of these species prefer to adsorb with their molecular planes either nearly parallel to the surface or significantly tilted with respect to the surface normal, allowing them to benefit from dispersion interactions with the metal surface. Nevertheless, some species adopt an upright orientation. The preference for flat-lying configurations can also be attributed to the low surface coverages considered in this study; it is well known that at higher coverages, molecules tend to orient upright. Additionally, more oxidized surfaces can favor upright over flat-lying orientations. Importantly, due to the thorough configurational search, CI-NEB calculations were also performed for the

---

[5] The reason only the C–S bond cleavages of thiolates were considered is that the corresponding reaction of S-$BimH_{(ads)}$ results in the same $BimH^{(C2)}_{(ads)}$ species **5** as in the C–S bond cleavage of Me-S-$BimH_{(ads)}$, reaction (10).

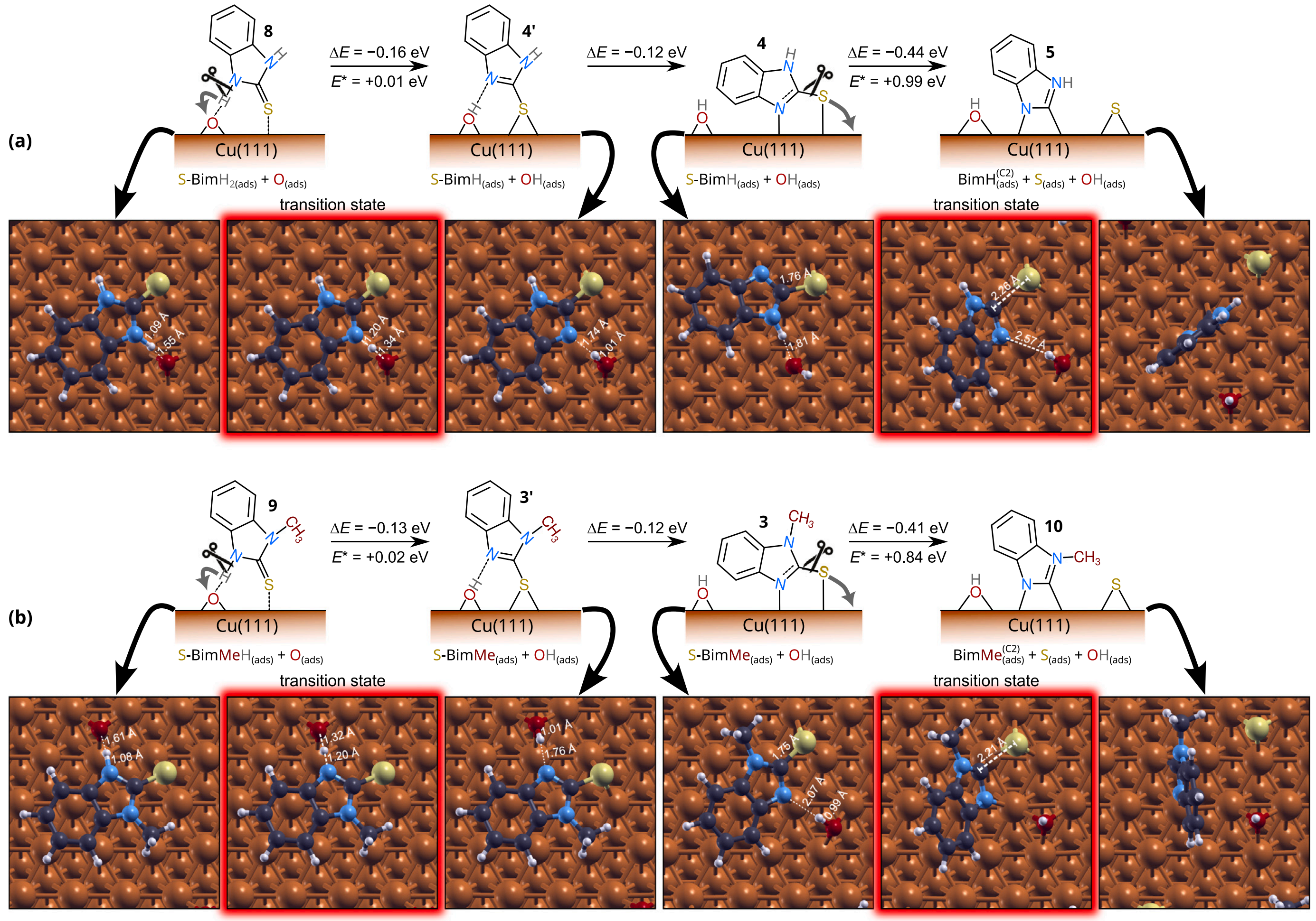

Fig. 9. Schematics and the corresponding snapshots of the most stable identified IS, TS, and FS structures for the considered surface reactions of (a) S-BimH$_{2(\mathrm{ads})}$ and (b) S-BimMeH$_{(\mathrm{ads})}$. The corresponding activation and reaction energies are also provided, while the bold numbers indicate the assigned identifiers of the adsorbed molecular species.

Table 2
Estimated mean reaction times (τ, in hours) for the considered reactions involving C–S bond cleavage. Values were derived using the calculated activation energies (E^*) and a frequency prefactor of $\nu = 10^{13}\ \mathrm{s}^{-1}$. Lower-bound ($\tau_{\min}$) and upper-bound ($\tau_{\max}$) estimates were obtained using Eqs. (18) and (19) with $\nu_{\max} = 100\nu$ and $\nu_{\min} = 0.01\nu$, respectively, and by accounting for an E^* uncertainty of ±0.1 eV. The τ, $\tau_{\min}$, and $\tau_{\max}$ values shorter than 100 h (maximum duration of the experiments) are highlighted in bold.

Reaction		E^* (eV)	τ (h)	$\tau_{\min}$ (h)	$\tau_{\max}$ (h)
(6)	Me-S-BimH → S-BimMeH	2.40	6e+23	1e+20	3e+27
(8)	Me-S-Bim$_{(\mathrm{ads})}$ + OH$_{(\mathrm{ads})}$ → S-BimMe$_{(\mathrm{ads})}$ + OH$_{(\mathrm{ads})}$	1.87	7e+14	2e+11	3e+18
(9)	Me-S-BimH$_{(\mathrm{ads})}$ + O$_{(\mathrm{ads})}$ → S-BimH$_{(\mathrm{ads})}$ + OMe$_{(\mathrm{ads})}$	1.47	1e+08	3e+04	7e+11
(10)	Me-S-BimH$_{(\mathrm{ads})}$ → BimH$^{(\mathrm{C2})}_{(\mathrm{ads})}$ + SMe$_{(\mathrm{ads})}$	0.85	**5e−03**	**1e−06**	**3e+01**
(11)	Me-S-Bim$_{(\mathrm{ads})}$ + O$_{(\mathrm{ads})}$ → S-Bim$_{(\mathrm{ads})}$ + OMe$_{(\mathrm{ads})}$	2.11	8e+18	2e+15	4e+22
(12)	Me-S-Bim$_{(\mathrm{ads})}$ → Bim$^{(\mathrm{C2})}_{(\mathrm{ads})}$ + SMe$_{(\mathrm{ads})}$	1.41	1e+07	3e+03	6e+10
(15)	S-BimH$_{(\mathrm{ads})}$ → BimH$^{(\mathrm{C2})}_{(\mathrm{ads})}$ + S$_{(\mathrm{ads})}$	0.99	**1e+00**	**2e−04**	6e+03
(16)	S-BimMe$_{(\mathrm{ads})}$ → BimMe$^{(\mathrm{C2})}_{(\mathrm{ads})}$ + S$_{(\mathrm{ads})}$	0.84	**5e−03**	**8e−07**	**2e+01**

upright configurations in most cases. A comparison between complementary IS, TS, and FS structures is presented in Figs. S1–S7 in the Supplementary material; in particular, when the most stable structure is nearly parallel to the surface, the complementary one is nearly perpendicular, and vice versa when the most stable structure is upright. Although the resulting energetics differ quantitatively, the qualitative picture discussed below remains largely unchanged, even when these less favorable complementary configurations are considered.

Among the ten qualitatively distinct adsorbed molecular species, Me-S-BimH and S-BimMeH share species **3** (S-BimMe$_{(\mathrm{ads})}$), while Me-S-BimH and S-BimH$_2$ share species **4** (S-BimH$_{(\mathrm{ads})}$) and **5** (BimH$^{(\mathrm{C2})}_{(\mathrm{ads})}$). This suggests a simple plausible explanation why these three molecular compounds show similar corrosion inhibition characteristics after several hours of immersion (cf. Fig. 4), i.e., molecular chemical transformations may lead to the same active species against corrosion, and the small differences between them may be attributed to the effect of different reaction co-products formed during these transformations. However, this inference is premature because, as already commented above, some transformations display activation barriers that are too high to be feasible at room temperature. For example, Me-S-BimH is unlikely to form species **3** and **4** due to the high reaction barrier, but it can form species **5** because its respective barrier is low enough. The criterion on which these claims are based stems from the Arrhenius equation,

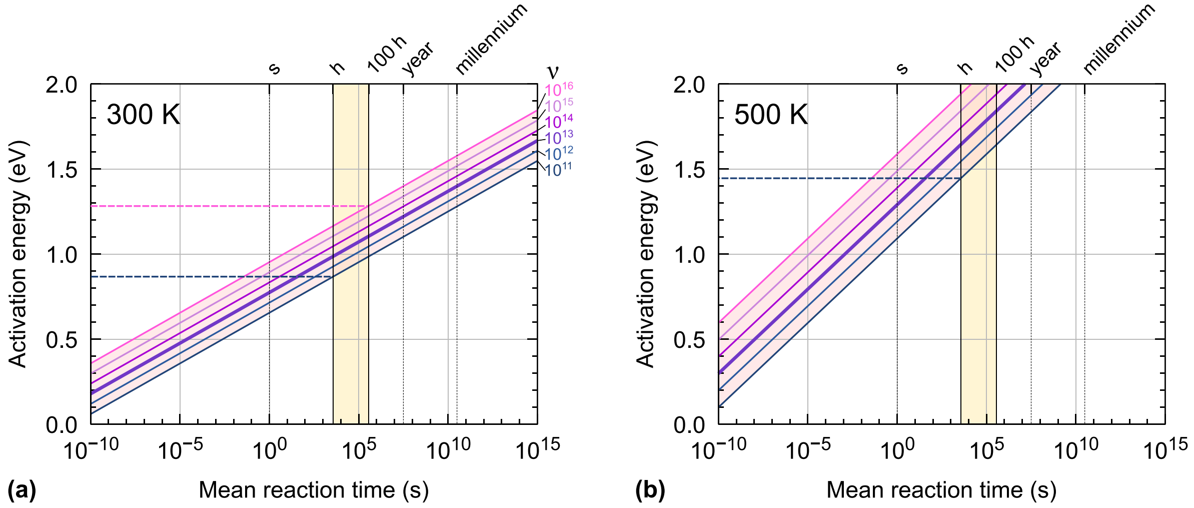

Fig. 10. The relationship between activation energy and mean reaction time at (a) 300 K and (b) 500 K, plotted for six values of the frequency prefactor, ranging from 10^{11} to 10^{16} s^{-1} in logarithmic increments. A vertical bright yellow band indicates the time interval corresponding to experimental measurements, performed after immersion times ranging from 1 h to 100 h. For a description of the horizontal dashed lines, see the main text.

according to which the average time (τ) for a reaction event[6] to occur — named *mean reaction time* for brevity — is given by:

$$\tau = \nu^{-1} \exp\left(\frac{E^*}{kT}\right), \tag{17}$$

where ν is the frequency prefactor (also named pre-exponential factor), E^* is the activation energy, k is the Boltzmann constant, and T is the temperature (at room temperature, $kT = 26$ meV). According to transition-state theory, the preexponential factor ν is related to the vibrational frequency of the initial state along the reaction coordinate (which is why it is called the *frequency prefactor*). For dissociation of adsorbed molecules, the frequency prefactors are often below or about the value of $kT/h \approx 10^{13}$ s^{-1} for $T \in [250, 700]$ K [36–38], where h is the Planck constant. In contrast, for desorption, the preexponential factors can be 1 to 3 orders of magnitude greater, reaching the values around 10^{16} s^{-1} [36,37,39–42].[7] On this basis, we adopt frequency prefactor values of 10^{13} and 10^{16} s^{-1} for surface dissociation reactions and desorption processes, respectively.

The above arguments are used to schematically present the feasibility of chemical reactions at 300 K (room temperature) and 500 K in Fig. 10, which depicts the relationship between activation energy and reaction mean time. A temperature of 300 K is chosen because the experiments were conducted at room temperature, whereas 500 K is used to illustrate the effect of temperature on reaction mean time. The relationship is shown for six values of the frequency prefactor, ranging from 10^{11} to 10^{16} s^{-1} in logarithmic increments. These values straddle the characteristic value of 10^{13} s^{-1}.

Experimental measurements were performed after immersion times ranging from 1 h to 100 h. Accordingly, we take 1 h and 100 h as characteristic times for dissociation reactions and inhibitors desorption, respectively, using prefactors of 10^{13} and 10^{16} s^{-1}. These times were chosen based on the following reasoning: the mean time for the dissociation reaction should not be excessively long for the reaction to be observable, whereas for the inhibitor to remain effective, it must persist on the surface throughout the experimental measurements. Consequently, Fig. 10a suggests that desorption barriers should be greater than 1.3 eV (marked with the horizontal pink dashed line) for the inhibitor to persist on the surface throughout the experimental measurements, whereas reaction barriers should be smaller than about 1.0 ± 0.1 eV for the reactions to be feasible at room temperature (the lower-bound of about 0.9 eV is marked by the horizontal bluish dashed line in the figure). The reaction feasibility claims in the Results section are based on this latter criterion. To illustrate the effect of temperature, Fig. 10b shows the relationship at the elevated temperature of 500 K: the resulting desorption and reaction barriers increase to about 2.1 and 1.7 eV.

To further substantiate the reaction feasibility claims presented in the Results section, Table 2 summarizes the estimated mean reaction times for the considered reactions involving C–S bond cleavage (reactions involving N–H bond cleavage are omitted from the table, as their marginal activation barriers render them evidently feasible under the experimental conditions). These estimates were obtained using Eq. (17), based on the calculated activation energies and assuming a frequency prefactor of $\nu = 10^{13}$ s^{-1}. To account for uncertainties in both the frequency prefactor and the activation energy, the table also includes lower-bound ($\tau_{\min}$) and upper-bound ($\tau_{\max}$) estimates. These bounds reflect a two-order-of-magnitude variation in the prefactor (i.e., $\nu_{\min} = 0.01\nu$ and $\nu_{\max} = 100\nu$), and an uncertainty of ± 0.1 eV in the activation energy. The resulting bounds were calculated using the modified expressions:

$$\tau_{\min} = \nu_{\max}^{-1} \exp\left(\frac{E^* - 0.1\ \text{eV}}{kT}\right) \tag{18}$$

and

$$\tau_{\max} = \nu_{\min}^{-1} \exp\left(\frac{E^* + 0.1\ \text{eV}}{kT}\right). \tag{19}$$

To summarize the adsorption energetics of Me-S-BimH and its subsequent chemical transformations, Fig. 11 schematically presents the corresponding reaction energy profile, with activation barriers for kinetically feasible (unfeasible) reaction steps at room temperature marked in green (red); the (un)feasibility classification is based on the criteria established in Fig. 10 and Table 2. The reaction energy profiles for the other two considered molecules, S-BimH$_2$ and S-BimMeH, are shown in Fig. 12. These figures reveal that the intact adsorbed molecules are the least stable, whereas their deprotonated counterparts are approximately 0.2–0.3 eV more stable. Further stabilization is achieved by cleaving the C–S bond between the azole ring and the S atom. The

---

[6] The reaction event itself is very fast (on the order of molecular vibrations), but it occurs very rarely.

[7] By analyzing desorption parameters for 133 molecules, Ligterink and Minissale [43] recently proposed the relationship $\log_{10}(\nu) = 2.65 \ln(m/m_0) + 8.07$, where m is the molecular mass in atomic mass units (amu) and $m_0 = 1$ amu. This relationship yields a frequency prefactor of approximately 10^{21} s^{-1} for the current molecules; however, we choose to use the more conventional value of 10^{16} s^{-1} instead.

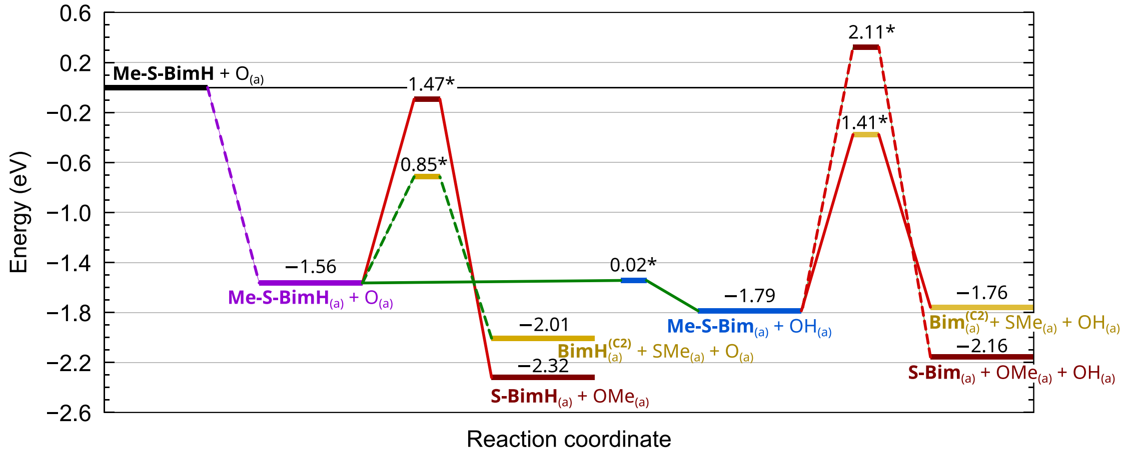

Fig. 11. Reaction energy profile for the adsorption of Me-S-BimH on O/Cu(111)–(4 × 4) and its subsequent chemical transformations considered in the Results section (reaction (8) is omitted). The reference zero energy corresponds to the isolated Me-S-BimH molecule and a bare O/Cu(111) substrate. Activation barriers for reaction steps that are kinetically feasible (unfeasible) at room temperature are marked with green (red) lines. Numbers followed by a star indicate the height of the reaction barrier, while the relative energy positions of the transition states can be determined directly from the graph.

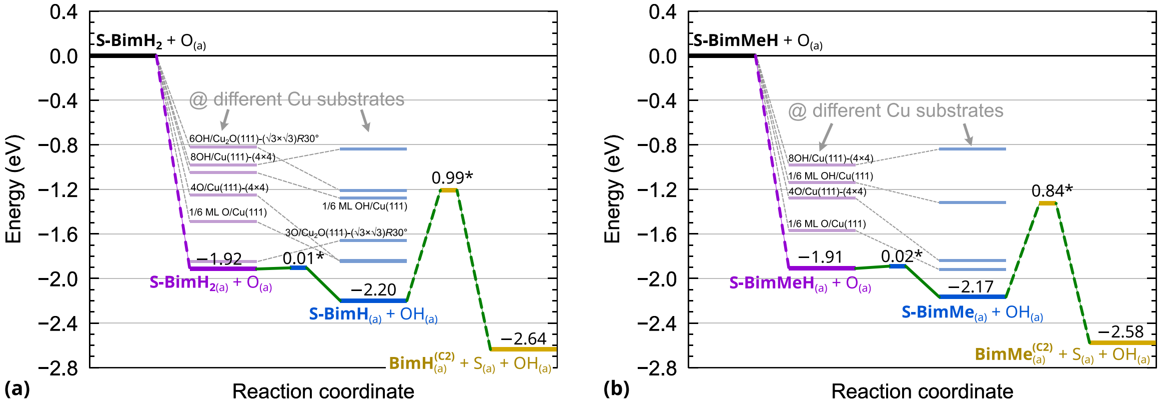

Fig. 12. Analogous to Fig. 11, but for (a) S-BimH$_2$ and (b) S-BimMeH. Additionally, the relative energy positions of adsorbed S-BimH$_2$/S-BimMeH and S-BimH/S-BimMe on various other Cu substrates, considered in Refs. [6,11], are indicated by pale purple and pale blue segments, respectively.

resulting $\mathrm{BimH}^{(C2)}_{(ads)}$ is about 0.5 and 0.9 eV more stable than intact Me-S-$\mathrm{BimH}_{(ads)}$ and S-$\mathrm{BimH}_{2(ads)}$, respectively, whereas $\mathrm{BimMe}^{(C2)}_{(ads)}$ is approximately 0.9 eV more stable than intact S-$\mathrm{BimMeH}_{(ads)}$.

It is evident from Figs. 11 and 12 that all adsorbed molecular species satisfy the condition that the desorption energy must be greater than about 1.3 eV for the molecules to persist on the surface during experimental measurements at room temperature. This explains why all three considered compounds act as corrosion inhibitors. However, it should be noted that a sufficiently strong molecule–surface bond is a necessary rather than sufficient condition for adsorption-type corrosion inhibitors. This aspect will be further examined below from another perspective, to which we now turn.

It is worth noting that for Me-S-$\mathrm{BimH}_{(ads)}$ and S-$\mathrm{BimH}_{(ads)}$, cleavage of the C–S bond between the azole ring and the S atom results in the formation of the $\mathrm{BimH}^{(C2)}_{(ads)}$ species **5** (cf. Figs. 7b and 9a). However, Figs. 11 and 12 reveal that the relative energy position of the corresponding adsorption state depends on the initial state, with values of −2.01 and −2.64 eV relative to isolated Me-S-BimH and S-BimH$_2$, respectively. This significant energy difference arises from the different reference states in each case. Nevertheless, it is reasonable to assume that once $\mathrm{BimH}^{(C2)}_{(ads)}$ forms, the two compounds should exhibit similar corrosion inhibition characteristics—an inference seemingly supported by experiments (cf. Fig. 4). Thus, while reaction energy profiles such as those shown in Figs. 11 and 12 are valuable for illustrating the thermodynamic and kinetic aspects of the considered reactions, they may not provide a complete picture. In particular, they overlook an aspect potentially relevant to corrosion inhibition, i.e., reaction energies do not directly reveal molecule–surface bond strengths (or binding energies). Instead, they represent cumulative energy changes, incorporating both bond-breaking and bond-making, except in the case of intact molecular adsorption, which involves only bond formation. For this reason, we present the molecule–surface binding energies of the involved molecular species in Table 3.

Table 3 reveals that deprotonated and C–S cleaved molecular species bind considerably more strongly to the surface than intact adsorbed molecules. The intact molecules bind to bare Cu(111) with energies ranging from −1.0 to −1.4 eV, while the presence of chemisorbed O atoms enhances molecule–surface bonding by approximately 0.5 eV due to hydrogen bond formation and strengthened N–Cu interaction [44]. Consequently, the binding energies of the intact molecules in this study range from −1.6 to −1.9 eV. Deprotonation increases binding strength by about 1 eV [31], with E_b values ranging from −2.8 to −3.2 eV. Molecules with a cleaved C–S bond exhibit even stronger binding, with E_b energies around −3.5 eV. The strongest binding is observed for doubly deprotonated C–S cleaved molecules, with binding energies between −3.9 and −4.6 eV. However, the last species are thermodynamically less favorable than their singly deprotonated C–S cleaved counterparts, implying that their enhanced molecule–surface

Table 3
Binding energies of adsorbed molecular species considered herein. Calculations were performed with one molecular species per Cu(111)–(4 × 4) supercell, either on bare Cu(111) or on Cu(111) precovered with O, OH, OMe, or SMe co-adsorbates. The label (X+Y)/Cu(111) indicates one X and one Y co-adsorbate per Cu(111)–(4 × 4) supercell.

species		substrate	E_b (eV)
intact			
1	Me-S-BimH$_{(ads)}$		
		Cu(111)	−1.02
		O/Cu(111)	−1.56
8	S-BimH$_{2(ads)}$		
		Cu(111)	−1.38
		O/Cu(111)	−1.92
9	S-BimMeH$_{(ads)}$		
		Cu(111)	−1.40
		O/Cu(111)	−1.91
deprotonated			
2	Me-S-Bim$_{(ads)}$		
		O/Cu(111)	−2.76
		OH/Cu(111)	−2.75
		(O+OH)/Cu(111)	−2.92
3	S-BimMe$_{(ads)}$		
		O/Cu(111)	−3.18
		OH/Cu(111)	−2.97
4	S-BimH$_{(ads)}$		
		O/Cu(111)	−3.22
		OH/Cu(111)	−2.96
		OMe/Cu(111)	−3.00
C–S cleaved and deprotonated			
5	$BimH^{(C2)}_{(ads)}$		
		(S+O)/Cu(111)	−3.47
		(S+OH)/Cu(111)	−3.40
		(SMe+O)/Cu(111)	−3.38
10	$BimMe^{(C2)}_{(ads)}$		
		O/Cu(111)	−3.41
		(S+OH)/Cu(111)	−3.42
C–S cleaved and doubly deprotonated			
6	S-Bim$_{(ads)}$		
		OMe/Cu(111)	−3.85
		(OMe+OH)/Cu(111)	−4.10
7	$Bim^{(C2)}_{(ads)}$		
		(SMe+O)/Cu(111)	−4.16
		(SMe+OH)/Cu(111)	−4.61

bond strength does not compensate for the additional intramolecular bond-breaking.

Inspection of Table 3 reveals that the E_b values depend on the substrate, which is both reasonable and expected. In this study, most calculations were performed on O/Cu(111)–(4 × 4), followed by OH/Cu(111)–(4 × 4), which forms from O/Cu(111) during molecular deprotonation. Bare Cu(111)–(4 × 4) and other coadsorbates thereon, such as OMe, S, and SMe, were also considered as they are reaction co-products. These coadsorbates can influence the binding energies by as much as 0.5 eV (cf. Table 3). How coadsorbates affect the molecular binding energies was scrutinized in our previous study [44], where three coadsorption effects were identified: (i) hydrogen bond formation, (ii) modifications of the direct molecule–surface bond (e.g., N–Cu), and (iii) coadsorbate-induced work function changes. Despite these notable differences, the binding energy trends are clearly evident, i.e., the molecule–surface bond strength follows the order: intact < deprotonated < C–S cleaved.

An even greater substrate effect on molecular adsorption energy, up to 1 eV, was observed in another study of ours [11], where various $Cu_2O(111)$-type substrate models were considered in addition to precovered Cu(111). Data from that study are utilized in Fig. 12, where the relative energy positions of intact S-BimH$_{2(ads)}$ and S-BimMeH$_{(ads)}$, as well as deprotonated S-BimH$_{(ads)}$ and S-BimMe$_{(ads)}$, on various Cu(111)- and $Cu_2O(111)$-type substrates are indicated by pale-purple and pale-blue line segments. Although the energy positions strongly depend on the substrate, deprotonated molecules are more stable than their intact counterparts in most cases. These observations suggest that the results presented in this study should be interpreted qualitatively, as precise values are highly sensitive to the chosen surface model. The qualitative trends are expected to hold across different Cu substrate models but are not universally valid, as shown by a few exceptions in Fig. 12.

Let us now continue our discussion of sufficiently strong molecule–surface bonding, which, as important as it may be, is by no means the only factor relevant to corrosion inhibition. Otherwise, chloride, which adsorbs strongly to copper substrates with bond strength above 3 eV [32,45], would be an excellent corrosion inhibitor, but is instead a prototypical corrosion activator. Consequently, a corrosion-inhibition analogue of the Sabatier principle was recently proposed [46], according to which the inhibitor should adsorb strongly enough to persist on the surface, but not so strongly that it promotes metal dissolution, as chlorides do. Nevertheless, adsorbed corrosion inhibitors should withstand being displaced by chlorides from the surface. It seems reasonable to assume that inhibitor species with molecule–surface bond strengths similar to that of Cl–Cu can better withstand chloride attack than those that bind more weakly.[8] In this context, Table 3 suggests that deprotonated and C–S cleaved molecular species, which bond with 3 eV or stronger, could better withstand chlorides than the intact molecules, which bond to the surface with less than 2 eV. This argument underscores the importance of molecular chemical transformations upon adsorption and explains why deprotonated and C–S cleaved species may play a crucial role in corrosion inhibition. In addition to the transformations of mercaptobenzimidazoles discussed above, other organic inhibitors may also undergo chemical changes upon adsorption. For example, triazoles and tetrazoles readily undergo N–H bond cleavage, resulting in more strongly bound species [31,32,49–51], whereas for imidazoles, cleavage of the C2–H bond is thermodynamically favored and kinetically feasible [31,52], although it is not as facile as N–H bond cleavage.

5. Conclusions

To prove or disprove the hypothesis that, for mercaptobenzimidazoles (such as the currently considered SH-BimH and SH-BimMe), the active molecular species inhibiting the corrosion of copper are thiolates — which adsorb significantly more strongly than the intact molecules — we performed corrosion experiments with 2-(methylthio) benzimidazole (Me-S-BimH), a mercaptobenzimidazole derivative in which the thiol group (–SH) is replaced with the methylthio group (–SCH_3). This modification should prevent the formation of surface thiolates. Corrosion experiments performed after 1 h of immersion in a 3 wt% aqueous NaCl solution reveal that Me-S-BimH is considerably less effective than SH-BimH and SH-BimMe in inhibiting copper corrosion. However, after 100 h of immersion, all three compounds function as effective mixed-type inhibitors with a stronger effect on the anodic branch, with Me-S-BimH outperforming SH-BimMe and, in particular, SH-BimH. This suggests that either the hypothesis that thiolates are the active species is incorrect, or some other molecular transformation activates Me-S-BimH over time. To investigate this possibility, we conducted a detailed DFT study of potential chemical transformations of adsorbed Me-S-BimH.

---

[8] It is worth noting that the competitive adsorption scenario is not the only way in which corrosion inhibitors can neutralize corrosion induced by chlorides. For surfactant inhibitors that form self-assembled organic layers, another mechanism was recently proposed [47,48]. Specifically, the self-assembled organic layer formed on the metallic substrate acts as a dielectric barrier, preventing chloride ions from penetrating it. This barrier mainly arises from the inferior solvation of ions in the organic layer compared to that in an aqueous solvent.

Most of the considered reactions are predicted to be exothermic, but only two display a sufficiently low activation barrier to be feasible at room temperature. The first is molecular deprotonation, assisted by a nearby adsorbed O atom (adsorbed OH would have a similar effect [31]), while the second is C–S bond cleavage between the azole ring and the methylthio group. Both reactions are exothermic and result in molecular species that bind to the surface considerably more strongly than the intact molecules. The other two studied molecules (SH-BimH and SH-BimMe) undergo analogous deprotonation and C–S bond cleavage reactions, also yielding more strongly adsorbed species. Interestingly, due to these chemical transformations, both Me-S-BimH and SH-BimH ultimately form the same $\mathrm{BimH}^{(C2)}_{(ads)}$ species, while SH-BimMe transforms into the analogous $\mathrm{BimMe}^{(C2)}_{(ads)}$ species. This finding may explain why, after an immersion period long enough for these species to form, all three compounds exhibit similar corrosion inhibition characteristics.

Our findings have important implications, as they help explain why it is so challenging to develop robust and predictive machine-learning models for screening new corrosion inhibitors. Such models are typically based on the molecular structures of the inhibitors, but if some molecules undergo chemical transformation upon adsorption while others do not, the models may struggle to provide accurate predictions, unless such chemical changes are explicitly incorporated into the models. Doing so can not only improve predictive reliability but also inspire the design of inhibitors that activate upon adsorption, enabling protection tailored for long-term corrosion resistance.

CRediT authorship contribution statement

Anton Kokalj: Writing – review & editing, Writing – original draft, Visualization, Supervision, Project administration, Methodology, Investigation, Funding acquisition, Formal analysis, Conceptualization. **Erik Gregori:** Writing – original draft, Visualization, Investigation. **Barbara Kapun:** Investigation. **Ingrid Milošev:** Writing – review & editing, Supervision, Methodology, Funding acquisition, Conceptualization.

Declaration of competing interest

The authors declare that they have no known competing financial interests or personal relationships that could have appeared to influence the work reported in this paper.

Acknowledgments

This work is a part of the M-Era.Net project entitled "Coin Desc: Corrosion inhibition and dealloying descriptors". The financial support of the project by MESS (Ministry of Education, Science and Sport of Republic of Slovenia, Grant No. C3330-17-500074) is acknowledged. This work has also been supported by the Slovenian Research and Innovation Agency (Grant No. P2-0393).

Appendix A. Supplementary data

Supplementary material related to this article can be found online at https://doi.org/10.1016/j.apsusc.2025.164139.

Data availability

The computational raw data required to reproduce these findings are available in the open-source online data repository hosted at Mendeley Data, in particular at https://doi.org/10.17632/yrcp4jk9z7.1.

References

[1] Y.I. Kuznetsov, L.P. Kazansky, Physicochemical aspects of metal protection by azoles as corrosion inhibitors, Russ. Chem. Rev. 77 (3) (2008) 219–232, http://dx.doi.org/10.1070/rc2008v077n03abeh003753.

[2] I. Milošev, N. Kovačević, J. Kovač, A. Kokalj, The roles of mercapto, benzene and methyl groups in the corrosion inhibition of imidazoles on copper: I. Experimental characterization, Corros. Sci. 98 (2015) 107–118, http://dx.doi.org/10.1016/j.corsci.2015.05.006, URL http://www.sciencedirect.com/science/article/pii/S0010938X15002000.

[3] A. Kokalj, M. Lozinšek, B. Kapun, P. Taheri, S. Neupane, P. Losada-Péez, C. Xie, S. Stavber, D. Crespo, F.U. Renner, A. Mol, I. Milošev, Simplistic correlations between molecular electronic properties and inhibition efficiencies: Do they really exist? Corros. Sci. 179 (2021) 108856, http://dx.doi.org/10.1016/j.corsci.2020.108856, URL https://www.sciencedirect.com/science/article/pii/S0010938X20307745.

[4] N. Kovačević, I. Milošev, A. Kokalj, The roles of mercapto, benzene, and methyl groups in the corrosion inhibition of imidazoles on copper: II. Inhibitor–copper bonding, Corros. Sci. 98 (2015) 457–470, http://dx.doi.org/10.1016/j.corsci.2015.05.041, URL http://www.sciencedirect.com/science/article/pii/S0010938X1500236X.

[5] I. Milošev, N. Kovačević, A. Kokalj, Effect of mercapto and methyl groups on the efficiency of imidazole and benzimidazole-based inhibitors of iron corrosion, Acta Chim. Slov. 63 (3) (2016) 544–559, http://dx.doi.org/10.17344/acsi.2016.2326, URL https://journals.matheo.si/index.php/ACSi/article/view/2326.

[6] D.K. Kozlica, A. Kokalj, I. Milošev, Synergistic effect of 2-mercaptobenzimidazole and octylphosphonic acid as corrosion inhibitors for copper and aluminium – An electrochemical, XPS, FTIR and DFT study, Corros. Sci. 182 (2021) 109082, http://dx.doi.org/10.1016/j.corsci.2020.109082, URL https://www.sciencedirect.com/science/article/pii/S0010938X20323635.

[7] S. Neupane, P. Losada-Pérez, U. Tiringer, P. Taheri, D. Desta, C. Xie, D. Crespo, A. Mol, I. Milošev, A. Kokalj, F.U. Renner, Study of mercaptobenzimidazoles as inhibitors for copper corrosion: Down to the molecular scale, J. Electrochem. Soc. 168 (5) (2021) 051504, http://dx.doi.org/10.1149/1945-7111/abf9c3, URL https://iopscience.iop.org/article/10.1149/1945-7111/abf9c3.

[8] E. Vernack, D. Costa, P. Tingaut, P. Marcus, DFT studies of 2-mercaptobenzothiazole and 2-mercaptobenzimidazole as corrosion inhibitors for copper, Corros. Sci. 174 (2020) 108840, http://dx.doi.org/10.1016/j.corsci.2020.108840, URL http://www.sciencedirect.com/science/article/pii/S0010938X19319225.

[9] F. Chiter, D. Costa, V. Maurice, P. Marcus, Adsorption of 2-mercaptobenzimidazole corrosion inhibitor on copper: DFT study on model oxidized interfaces, J. Electrochem. Soc. 167 (16) (2020) 161506, http://dx.doi.org/10.1149/1945-7111/abcd4f, URL https://iopscience.iop.org/article/10.1149/1945-7111/abcd4f.

[10] F. Chiter, D. Costa, V. Maurice, P. Marcus, Atomic scale insight into corrosion inhibition: DFT study of 2-mercaptobenzimidazole on locally de-passivated copper surfaces, J. Electrochem. Soc. 168 (12) (2021) 121507, http://dx.doi.org/10.1149/1945-7111/ac405c.

[11] I. Milošev, P. Taheri, B. Kapun, D.K. Kozlica, A. Mol, A. Kokalj, The effect of molecular structure of imidazole-based compounds on corrosion inhibition of Cu, Zn, and Cu-Zn alloys, Corros. Sci. 240 (2024) 112328, http://dx.doi.org/10.1016/j.corsci.2024.112328.

[12] A. Kokalj, P. Gava, S. de Gironcoli, S. Baroni, What determines the catalyst's selectivity in the ethylene epoxidation reaction, J. Catal. 254 (2) (2008) 304–309, http://dx.doi.org/10.1016/j.jcat.2008.01.008, URL http://www.sciencedirect.com/science/article/pii/S0021951708000134.

[13] P. Giannozzi, S. Baroni, N. Bonini, M. Calandra, R. Car, C. Cavazzoni, D. Ceresoli, G.L. Chiarotti, M. Cococcioni, I. Dabo, A. Dal Corso, S. de Gironcoli, S. Fabris, G. Fratesi, R. Gebauer, U. Gerstmann, C. Gougoussis, A. Kokalj, M. Lazzeri, L. Martin-Samos, N. Marzari, F. Mauri, R. Mazzarello, S. Paolini, A. Pasquarello, L. Paulatto, C. Sbraccia, S. Scandolo, G. Sclauzero, A.P. Seitsonen, A. Smogunov, P. Umari, R.M. Wentzcovitch, Quantum ESPRESSO: a modular and open-source software project for quantum simulations of materials, J. Phys.: Condens. Matter. 21 (39) (2009) 395502, http://dx.doi.org/10.1088/0953-8984/21/39/395502, code available from http://www.quantum-espresso.org/. URL https://iopscience.iop.org/article/10.1088/0953-8984/21/39/395502.

[14] P. Giannozzi, O. Andreussi, T. Brumme, O. Bunau, M.B. Nardelli, M. Calandra, R. Car, C. Cavazzoni, D. Ceresoli, M. Cococcioni, N. Colonna, I. Carnimeo, A.D. Corso, S. de Gironcoli, P. Delugas, R. DiStasio, A. Ferretti, A. Floris, G. Fratesi, G. Fugallo, R. Gebauer, U. Gerstmann, F. Giustino, T. Gorni, J. Jia, M. Kawamura, H.-Y. Ko, A. Kokalj, E. Küçükbenli, M. Lazzeri, M. Marsili, N. Marzari, F. Mauri, N.L. Nguyen, H.-V. Nguyen, A.O. de-la Roza, L. Paulatto, S. Poncé, D. Rocca, R. Sabatini, B. Santra, M. Schlipf, A.P. Seitsonen, A. Smogunov, I. Timrov, T. Thonhauser, P. Umari, N. Vast, X. Wu, S. Baroni, Advanced capabilities for materials modelling with Quantum ESPRESSO, J. Phys.: Condens. Matter. 29 (2017) 465901, http://dx.doi.org/10.1088/1361-648X/aa8f79, URL http://iopscience.iop.org/10.1088/1361-648X/aa8f79.

[15] D. Gustinčič, A. Kokalj, A DFT study of adsorption of imidazole, triazole, and tetrazole on oxidized copper surfaces: $Cu_2O(111)$ and $Cu_2O(111)$-w/o-Cu^{CUS}, Phys. Chem. Chem. Phys 17 (2015) 28602–28615, http://dx.doi.org/10.1039/C5CP03647J.

[16] J.P. Perdew, K. Burke, M. Ernzerhof, Generalized gradient approximation made simple, Phys. Rev. Lett. 77 (18) (1996) 3865–3868, http://dx.doi.org/10.1103/PhysRevLett.77.3865, URL https://journals.aps.org/prl/abstract/10.1103/PhysRevLett.77.3865.

[17] S. Grimme, Semiempirical GGA-type density functional constructed with a long-range dispersion correction, J. Comput. Chem. 27 (15) (2006) 1787–1799, http://dx.doi.org/10.1002/jcc.20495, URL https://onlinelibrary.wiley.com/doi/10.1002/jcc.20495.

[18] E.R. McNellis, J. Meyer, K. Reuter, Azobenzene at coinage metal surfaces: Role of dispersive van der Waals interactions, Phys. Rev. B 80 (2009) 205414, http://dx.doi.org/10.1103/PhysRevB.80.205414, URL http://link.aps.org/doi/10.1103/PhysRevB.80.205414.

[19] K. Tonigold, A. Groß, Adsorption of small aromatic molecules on the (111) surfaces of noble metals: A density functional theory study with semiempirical corrections for dispersion effects, J. Chem. Phys. 132 (22) (2010) 224701, http://dx.doi.org/10.1063/1.3439691, URL http://link.aip.org/link/?JCP/132/224701/1.

[20] A. Kokalj, S. Peljhan, Density functional theory study of ATA, BTAH, and BTAOH as copper corrosion inhibitors: Adsorption onto Cu(111) from gas phase, Langmuir 26 (18) (2010) 14582–14593, http://dx.doi.org/10.1021/la1019789, URL http://pubs.acs.org/doi/abs/10.1021/la1019789.

[21] A. Kokalj, PWTK: PWScf ToolKit, 2024, code available from http://pwtk.ijs.si/.

[22] A. Kokalj, XCrySDen—a new program for displaying crystalline structures and electron densities, J. Mol. Graph. Model. 17 (1999) 176–179, http://dx.doi.org/10.1016/S1093-3263(99)00028-5, code available from http://www.xcrysden.org/.

[23] Inkscape Project, Inkscape, 2021, version 1.0.2 https://inkscape.org.

[24] H.J. Monkhorst, J.D. Pack, Special points for Brillouin-zone integrations, Phys. Rev. B 13 (12) (1976) 5188–5192, http://dx.doi.org/10.1103/PhysRevB.13.5188, URL https://journals.aps.org/prb/abstract/10.1103/PhysRevB.13.5188.

[25] M. Methfessel, A.T. Paxton, High-precision sampling for Brillouin-zone integration in metals, Phys. Rev. B 40 (1989) 3616–3621, http://dx.doi.org/10.1103/PhysRevB.40.3616, URL http://link.aps.org/doi/10.1103/PhysRevB.40.3616.

[26] I.B. Obot, D.D. Macdonald, Z.M. Gasem, Density functional theory (DFT) as a powerful tool for designing new organic corrosion inhibitors. Part 1: An overview, Corros. Sci. 99 (2015) 1–30, http://dx.doi.org/10.1016/j.corsci.2015.01.037, URL http://www.sciencedirect.com/science/article/pii/S0010938X15000487.

[27] G. Henkelman, H. Jónsson, Improved tangent estimate in the nudged elastic band method for finding minimum energy paths and saddle points, J. Chem. Phys. 113 (22) (2000) 9978–9985, http://dx.doi.org/10.1063/1.1323224, URL https://aip.scitation.org/doi/abs/10.1063/1.1323224.

[28] G. Henkelman, B.P. Uberuaga, H. Jónsson, A climbing image nudged elastic band method for finding saddle points and minimum energy paths, J. Chem. Phys. 113 (22) (2000) 9901–9904, http://dx.doi.org/10.1063/1.1329672, URL https://aip.scitation.org/doi/abs/10.1063/1.1329672.

[29] C. Xie, I. Milošev, A. Kokalj, P. Bruna, D. Crespo, Imidazole- and mercaptobenzimidazole-derivatives as corrosion inhibitors for Cu, Cu–Zn alloys, and Zn in chloride solution, Electrochim. Acta 532 (2025) 146460, http://dx.doi.org/10.1016/j.electacta.2025.146460.

[30] A. Kokalj, S. Peljhan, J. Koller, The effect of surface geometry of copper on dehydrogenation of benzotriazole. Part II, J. Phys. Chem. C 118 (2) (2014) 944–954, http://dx.doi.org/10.1021/jp409719, URL http://pubs.acs.org/doi/abs/10.1021/jp409719c.

[31] A. Kokalj, M. Dlouhy, Dissociative adsorption of azoles on Cu(111) promoted by chemisorbed O and OH, Corros. Sci. 209 (2022) (2022) 110680, http://dx.doi.org/10.1016/j.corsci.2022.110680.

[32] D. Gustinčič, A. Kokalj, DFT study of azole corrosion inhibitors on Cu_2O model of oxidized copper surfaces: I. Molecule–surface and Cl–surface bonding, Metals 8 (5) (2018) 310, URL http://www.mdpi.com/2075-4701/8/5/310.

[33] X. Wu, F. Wiame, V. Maurice, P. Marcus, 2-Mercaptobenzimidazole films formed at ultra-low pressure on copper: adsorption, thermal stability and corrosion inhibition performance, Appl. Surf. Sci. 527 (2020) 146814, http://dx.doi.org/10.1016/j.apsusc.2020.146814.

[34] L. Ruan, I. Stensgaard, F. Besenbacher, E. Lægsgaard, A scanning tunneling microscopy study of the interaction of S with the Cu(111) surface, Ultramicroscopy 42-44 (1992) 498–504, http://dx.doi.org/10.1016/0304-3991(92)90313-9.

[35] X. Wu, F. Wiame, V. Maurice, P. Marcus, Adsorption and thermal stability of 2-mercaptobenzothiazole corrosion inhibitor on metallic and pre-oxidized Cu(111) model surfaces, Appl. Surf. Sci. 508 (2019) 145132, http://dx.doi.org/10.1016/j.apsusc.2019.145132.

[36] C.T. Campbell, Y.-K. Sun, W. Weinberg, Trends in preexponential factors and activation energies in dehydrogenation and dissociation of adsorbed species, Chem. Phys. Lett. 179 (1991) 53–57, http://dx.doi.org/10.1016/0009-2614(91)90290, URL http://www.sciencedirect.com/science/article/pii/000926149190290P.

[37] R.C. Baetzold, G.A. Somorjai, Preexponential factors in surface reactions, J. Catal. 45 (1) (1976) 94–105, http://dx.doi.org/10.1016/0021-9517(76)90059-2.

[38] D. Mei, L. Xu, G. Henkelman, Potential energy surface of methanol decomposition on Cu(110), J. Phys. Chem. C 113 (11) (2009) 4522–4537, http://dx.doi.org/10.1021/jp808211q, arXiv:http://pubs.acs.org/doi/pdf/10.1021/jp808211q. URL http://pubs.acs.org/doi/abs/10.1021/jp808211q.

[39] V. Zhdanov, Arrhenius parameters for rate processes on solid surfaces, Surf. Sci. Rep. 12 (5) (1991) 185–242, http://dx.doi.org/10.1016/0167-5729(91)90011-L.

[40] S.L. Tait, Z. Dohnálek, C.T. Campbell, B.D. Kay, *n*-alkanes on Pt(111) and on C(0001)/Pt(111): Chain length dependence of kinetic desorption parameters, J. Chem. Phys. 125 (23) (2006) 234308, http://dx.doi.org/10.1063/1.2400235, URL http://link.aip.org/link/?JCP/125/234308/1.

[41] K.A. Fichthorn, R.A. Miron, Thermal desorption of large molecules from solid surfaces, Phys. Rev. Lett. 89 (2002) 196103, http://dx.doi.org/10.1103/PhysRevLett.89.196103, URL http://link.aps.org/doi/10.1103/PhysRevLett.89.196103.

[42] M.N. Rocklein, T.V. Arnold, C.M. Gerth, D.P. Land, The desorption kinetics of flat-lying benzene from palladium (111), J. Phys. Chem. B 108 (3) (2004) 1009–1013, http://dx.doi.org/10.1021/jp036038, URL http://pubs.acs.org/doi/abs/10.1021/jp036038q.

[43] N.F.W. Ligterink, M. Minissale, Overview of desorption parameters of volatile and complex organic molecules – A systematic dig through the experimental literature, Astron. Astrophys. 676 (2023) A80, http://dx.doi.org/10.1051/0004-6361/202346436.

[44] M. Dlouhy, A. Kokalj, How adsorbed H O, OH, and Cl affect plain adsorption of imidazole on copper, Corros. Sci. 205 (2022) (2022) 110443, http://dx.doi.org/10.1016/j.corsci.2022.110443.

[45] S. Peljhan, A. Kokalj, Adsorption of chlorine on Cu(111): A density-functional theory study, J. Phys. Chem. C 113 (32) (2009) 14363–14376, http://dx.doi.org/10.1021/jp902273k.

[46] A. Kokalj, Corrosion inhibitors: physisorbed or chemisorbed? Corros. Sci. 196 (2022) 109939, http://dx.doi.org/10.1016/j.corsci.2021.109939.

[47] A. Kokalj, D. Costa, Model study of penetration of Cl^- ions from solution into organic self-assembled-monolayer on metal substrate: Trends and modeling aspects, J. Electrochem. Soc. 168 (7) (2021) 071508, http://dx.doi.org/10.1149/ac0a24, URL https://iopscience.iop.org/article/10.1149/1945-7111/ac0a24.

[48] F. Chiter, D. Costa, M. Poberžnik, I. Milošev, P. Marcus, A. Kokalj, DFT study of Cl^- ingress into organic self-assembled monolayers on aluminum, J. Electrochem. Soc. 170 (7) (2023) 071504, http://dx.doi.org/10.1149//ace334, URL https://iopscience.iop.org/article/10.1149/1945-7111/ace334.

[49] S. Peljhan, J. Koller, A. Kokalj, The effect of surface geometry of copper on adsorption of benzotriazole and Cl. Part I, J. Phys. Chem. C 118 (2) (2014) 933–943, http://dx.doi.org/10.1021/jp409717, URL http://pubs.acs.org/doi/abs/10.1021/jp409717e.

[50] N. Kovačević, A. Kokalj, The relation between adsorption bonding and corrosion inhibition of azole molecules on copper, Corros. Sci. 73 (2013) 7–17, http://dx.doi.org/10.1016/j.corsci.2013.03.016, URL http://www.sciencedirect.com/science/article/pii/S0010938X13000954.

[51] N. Kovačević, I. Milošev, A. Kokalj, How relevant is the adsorption bonding of imidazoles and triazoles for their corrosion inhibition of copper? Corros. Sci. 124 (2017) 25–34, http://dx.doi.org/10.1016/j.corsci.2017.04.021, URL http://www.sciencedirect.com/science/article/pii/S0010938X16307715.

[52] A. Kokalj, D. Gustinčič, M. Poberžnik, M. Lozinšek, New insights into adsorption bonding of imidazole: A viable C2–H bond cleavage on copper surfaces, Appl. Surf. Sci. 479 (2019) 463–468, http://dx.doi.org/10.1016/j.apsusc.2018.12.246, URL http://www.sciencedirect.com/science/article/pii/S0169433218335943.